

Band Visibility in High-Resolution Optical Coherence Tomography Assessed With a Custom Review Tool and Updated, Histology-Derived Nomenclature

Lukas Goerdt^{1,2}, Thomas A. Swain¹, Deepayan Kar¹, Gerald McGwin^{1,3}, Andreas Berlin^{1,4}, Mark E. Clark¹, Cynthia Owsley¹, Kenneth R. Sloan¹, and Christine A. Curcio¹

¹ Department of Ophthalmology and Visual Sciences, University of Alabama at Birmingham, Heersink School of Medicine, Birmingham, AL, USA

² Department of Ophthalmology, University of Bonn, Bonn, Germany

³ Department of Epidemiology, School of Public Health, University of Alabama at Birmingham, AL, USA

⁴ Department of Ophthalmology, University of Würzburg, Würzburg, Germany

Correspondence: Christine A. Curcio, Department of Ophthalmology and Visual Sciences; University of Alabama at Birmingham Heersink School of Medicine, Birmingham, AL 35294-0019, USA.

e-mail cacurcio@gmail.com

Received: August 13, 2024

Accepted: November 16, 2024

Published: December 13, 2024

Keywords: optical coherency tomography; high-resolution; nomenclature; Mie scattering; organelles; review software; volume electron microscopy; age-related macular degeneration

Citation: Goerdt L, Swain TA, Kar D, McGwin G, Berlin A, Clark ME, Owsley C, Sloan KR, Curcio CA. Band visibility in high-resolution optical coherence tomography assessed with a custom review tool and updated, histology-derived nomenclature. *Transl Vis Sci Technol*. 2024;13(12):19, <https://doi.org/10.1167/tvst.13.12.19>

Purpose: For structure-function research at the transition of aging to age-related macular degeneration, we refined the current consensus optical coherence tomography (OCT) nomenclature and evaluated a novel review software for investigational high-resolution OCT imaging (HR-OCT; <3 μm axial resolution).

Method: Volume electron microscopy, immunolocalizations, histology, and investigational devices informed a refined OCT nomenclature for a custom ImageJ-based review tool to assess retinal band visibility. We examined effects on retinal band visibility of automated real-time averaging (ART) 9 and 100 (11 eyes of 10 healthy young adults), aging (10 young vs 22 healthy aged), and age-related macular degeneration (AMD; 22 healthy aged, 17 early (e)AMD, 15 intermediate (i)AMD). Intrareader reliability was assessed.

Results: Bands not included in consensus nomenclature are now visible using HR-OCT: inner plexiform layer (IPL) 1-5, outer plexiform layer (OPL) 1-2, outer segment interdigitation zone 1-2 (OSIZ, including hyporeflective outer segments), and retinal pigment epithelium (RPE) 1-5. Cohen's kappa was 0.54–0.88 for inner and 0.67–0.83 for outer retinal bands in a subset of 10 eyes. IPL-3-5 and OPL-2 visibility benefitted from increased ART. OSIZ-2 and RPE-1,2,3,5 visibility was worse in aged eyes than in young eyes. OSIZ-1-2, RPE-1, and RPE-5 visibility decreased in eAMD and iAMD compared to healthy aged eyes.

Conclusions: We reliably identified 28 retinal bands using a novel review tool for HR-OCT. Image averaging improved inner retinal band visibility. Aging and AMD development impacted outer retinal band visibility.

Translational Significance: Detailed knowledge of anatomic structures visible on OCT will enhance precision in research, including AI training and structure-function analyses.

Introduction

Spectral domain optical coherence tomography (SD-OCT) of the retina reveals alternating bands of relative hyper- and hyporeflectivity generated by

boundaries between differing indices of refraction.¹ These partially overlap with the layers of classic histology.² Light scattering (i.e., light redirection from an incident direction) can occur at water-lipid interfaces such as the surfaces of membrane-bounded organelles.³ Organelles with diameter larger than or



equal to the wavelength of light ($\sim 1 \mu\text{m}$) can modulate OCT reflectivity, according to Mie theory.^{4–7} In the outer retina, organelles of 100 million photoreceptors (up to $140 \mu\text{m}$ tall in the central area)⁸ are vertically compartmentalized and horizontally aligned, creating the distinctive outer retinal reflective bands of OCT. This compartmentalization also applies to the retinal pigment epithelium (RPE; cell bodies, $14 \mu\text{m}$ tall), where lysosome-related organelles (melanosomes, lipofuscin, and melanolipofuscin) and mitochondria form precisely stacked cushions that contribute reflectivity.^{9–11}

In the last decade, histologic studies of aged human eyes with and without age-related macular degeneration (AMD), some with *in vivo* clinical imaging, have elucidated signal sources in clinical OCT, and these substantiate a need for higher axial resolution.⁵ Photoreceptor mitochondria are highly reflective per se. This reflectivity increases further during degenerative fission and inward translocation that effectively shortens the inner segment (IS) myoids.^{12,13} Basal laminar deposit (BLamD) is a thickened basement membrane material (mean thickness, $6 \mu\text{m}$) internal to the native RPE basal lamina. BLamD is hyporeflective if RPE is intact and shadowing, hyperreflective if RPE has atrophied, and relevant to treatment decisions about anti-angiogenic medications.¹⁴ Soft drusen are the major intraocular risk factor for AMD progression.^{15,16} Yet a clinically invisible layer of the same material, basal linear deposit (BLinD, $2 \mu\text{m}$ thick), surrounds visible drusen and may also increase risk for type 1 macular neovascularization, for persons of European^{17–19} and possibly Asian ancestry.¹⁹ BLamD and BLinD have not yet been investigated longitudinally on OCT; BLinD is thus far invisible in routine clinical imaging.²⁰

Evolving resolution and analytics on investigational OCT devices have disclosed previously non-visible bands that could imminently accelerate research if rigorously assessed.^{21–24} Near-histologic detail enables the discovery of structural changes before disease manifests and increases the reliability of layer segmentation and biomarker identification.^{25–27} Artificial intelligence approaches using machine and deep learning (DL) techniques hold promise for automated identification of predictive OCT biomarkers for AMD end-stages.^{28–35} Development and training required for the retinal structures in question may benefit from higher-resolution training data.

In 2021 a novel investigational High-Resolution OCT device (herein called “High-Res OCT”) was released by Heidelberg Engineering (Heidelberg, Germany), with key modifications of the existing SD-OCT Spectralis platform. Axial resolution improved from $7 \mu\text{m}$ to $<3 \mu\text{m}$ (optical) due to two modifi-

cations: increasing the spectral bandwidth (from 50 nm to 137 nm) of the super luminescent light source and shortening the central wavelength (from 880 nm to 853 nm).^{25,36} The device-specific review software Heidelberg EyeExplorer (Heyex) was not modified to facilitate annotations beyond a default 11-layer segmentation. In the context of developing new review software for our studies, we also revisited the 2014 consensus OCT nomenclature for SD-OCT.²⁰ The present study proposes a nomenclature for $<3 \mu\text{m}$ axial resolution OCT devices (referred to as “ $<3 \mu\text{m}$ OCT”)³⁷ and introduces a custom review and annotation tool for OCT imaging that also serves as an initial validation of the nomenclature.

Methods

Overview

A 2014 SD-OCT nomenclature by Staurenghi et al.²⁰ (IN-OCT) evolved from an extensive review of histologic data² followed by a roundtable meeting. This scheme supported new terminology for AMD by the Classification of Atrophy Meetings group.^{38–40} Because of its overall accuracy, solid grounding in histology, and eventual wide acceptance, we chose to adopt and refine this nomenclature. As the originators anticipated, some aspects can be reevaluated, considering new data. For example, the RPE/Bruch membrane complex was termed a single band. Structures known from histology such as the RPE basal lamina (BL), BLamD, and type 1 neovascularization are now visible within this complex.^{14,41} Some hyporeflective bands, including one between the ellipsoid zone (EZ) and interdigitation zone (IZ) containing outer segments (OS), were not named. A hyporeflective band between the IZ and the RPE-Bruch membrane complex has since been recognized.^{22,42,43}

In the long term, our research group seeks correlations between retinal structure and visual function that can support interventions and treatments for AMD at stages before atrophy. Our underlying hypothesis is a Center-Surround model of cone resilience and rod vulnerability that is anchored by a precisely defined foveal center.⁴⁴ These goals inform our choices in the design of review software, as described below.

Guiding Principles for Nomenclature Development

We followed several technical and biological principles to ensure universality, applicability, and flexibility for future development. Detail about supporting histology is provided in the Discussion.

1. Incorporate existing consensus nomenclature,²⁰ wherever possible.
2. For consistency, name all bands according to the respective posterior boundary, as done for inner retina. Some IN-OCT bands were treated as lines, which do not have thicknesses. Bands have measurable thicknesses.
3. Determine whether known anatomical structures can be reliably seen in a clinically feasible setting (e.g., ART = 9). Those that cannot be reliably seen should be accommodated in nomenclature to allow their future visibility, as technology improves.
4. Use numbers to designate sub-bands, especially those in need of further anatomical information.
5. Generate uniformly structured output of variables to facilitate data processing and compilation for analysis in batch mode.
6. Incorporate data from immunolocalization studies of neurotransmission and neuromodulation proteins showing five sub-layers in the IPL (three inner for ON pathway, two outer for OFF pathway),^{24,45,46} as already correlated to bands of alternating reflectivity in OCT.⁴⁷
7. Incorporate new information from High Res-OCT supporting two reflective bands in the outer plexiform layer (OPL),²¹ in apparent correspondence to layers of mitochondria visualized by volume electron microscopy (Figs. 5 and 3 of reference 21, respectively). OPL contains synaptic terminals of photoreceptors and connecting processes of interneurons.
8. Incorporate a proposed OS-IZ complex²² of which the OS can be subdivided roughly into thirds. The anterior hyporeflective third, unnamed in IN-OCT, corresponds to bare photoreceptor OS (i.e., not covered by apical processes). The posterior hyperreflective two-thirds corresponds to photoreceptor OS covered by RPE apical processes.¹¹
9. Incorporate results from volume electron microscopy showing multiple organelle layers in the RPE (melanosomes in apical processes (OSIZ-2), melanolipofuscin and lipofuscin concentrated in the middle of the cell body (RPE-2), and mitochondria concentrated at the basal portion (RPE-4),^{11,48} as shown Figure 1 of reference 11).
10. Incorporate new information from $<3\text{ }\mu\text{m}$ axial resolution OCT devices showing a hyporeflective band at the base of the RPE cell body. This is attributed to basal infoldings or BLamD, in young versus aged adults, respectively.^{23,49}
11. Incorporate new information from AMD histology, including direct clinicopathologic correlation, highlighting the potential visibility of extracellular deposits of prognostic value on either side of the RPE.^{14,18,40,50-53}
12. Define the foveal center as the point where cone photoreceptors are at their longest, in the central bouquet.⁵⁴ This is where cones and possibly also Müller glia are at their highest spatial densities.⁵⁵

Nomenclature for $<3\text{ }\mu\text{m}$ Resolution OCT

We identified 28 retinal bands, separated by 27 retinal boundaries (Figs. 1, 2). Bands added to the IN-OCT nomenclature are IPL bands 1-5,²⁴ OPL bands 1-2,²¹ OS and apical processes (IZ) bands 1-2,²² and RPE bands 1-5.¹¹ Figure 1 schematizes the nomenclature and groups bands according to organizational principles in retinal neurophysiology, vascular biology, and embryology. Figure 2 represents its application in vivo in a healthy 34-year-old man, with a representative longitudinal reflectivity profile (LRP), and details the location of the central bouquet. The LRP is a graphical representation of gray-scale values (0-255, black to white) along one or more adjacent A-scans from anterior to posterior. These align well with the underlying anatomical structures.⁵⁶⁻⁵⁸ Herein three adjacent A-scans were averaged for each LRP, where the middle A-scan represents the location of the grading. Figures 3, 4, and 5 provide examples of a healthy aged eye, early (e)AMD eye, and an intermediate (i)AMD eye, respectively.

Custom OCT Review Tool

A current unmet need is OCT review software that allows for the manual assessment of all visible retinal bands. We addressed this need with a custom review tool (Fig. 6)⁵⁹ called “Retinal Bands 2024”, an ImageJ plug-in⁶⁰ that is freely available at <https://sites.imagej.net/CreativeComputation/>.

Plug-in operation is detailed in the Supplementary Material. A prerequisite is manual placement of the foveal center at the inward rise of the external limiting membrane (ELM) and EZ, using the plug-in “Find Fovea OCT”. “Retinal Bands 2024” directs the user to every retinal band at nine eccentricities (-2.5 mm to 2.5 mm), in horizontally oriented B-scans at two retinal locations (foveal center, 5° superior retina, Fig. 7). Because of the steep gradient of cone density within the foveola,^{44,61} this region has three assessment locations (-0.1, 0.0, 0.1 mm). At every location, the user is required to judge whether a band is visible on the OCT scan and the LRP at that A-scan, as well as to deter-

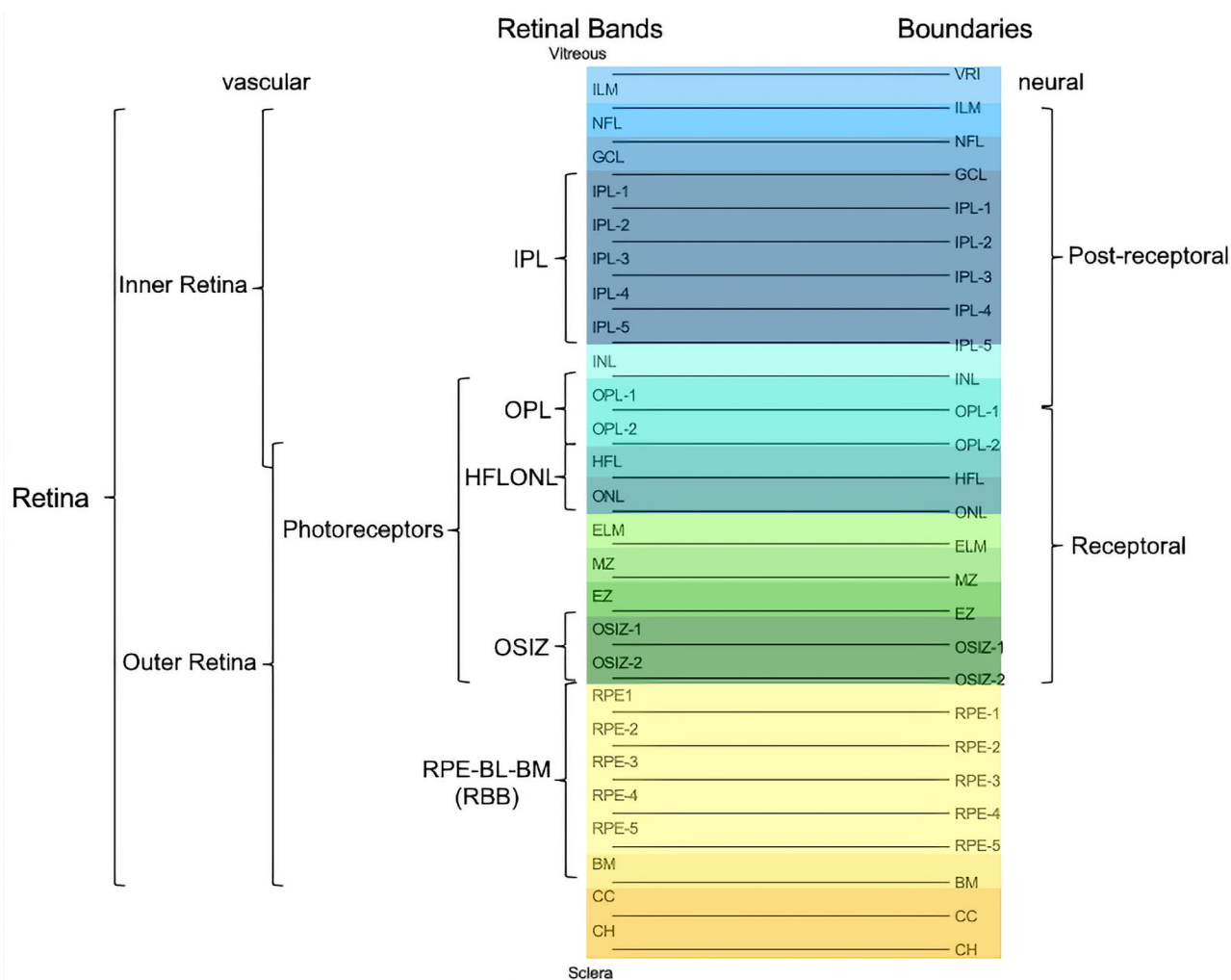


Figure 1. Simplified presentation of the proposed High-Resolution Optical Coherence Tomography nomenclature. Overview of the retinal bands and boundaries for the proposed HR-OCT nomenclature. A total of 28 retinal bands (including the vitreous and the sclera) and 27 boundaries are included. Photoreceptors range from OPL-1 to OSIZ-2. Post-receptoral retina contains bipolar cells and ganglion cells, which form multiple parallel pathways to the brain, represented by bands between ILM and INL; these bands also contain horizontal cells and amacrine cells that modulate signals along these pathways. The inner retina (blue) combines all layers from the ILM to the OPL-2, which are supplied by the vascular plexuses; these have a barrier function analogous to the cerebral vasculature. The outer retina (teal, green, yellow) contains all bands from the OPL-2 to Bruch membrane, representing cells supplied by the choroid (orange), a specialized bed of systemic circulation.¹²⁶ BM, Bruch membrane; CC, choriocapillaris; CH, choroid. GCL, ganglion cell layer; HFL, Henle fiber layer; IPL, inner plexiform layer; ILM, internal limiting membrane; MZ, myoid zone; NFL, nerve fiber layer; OPL, outer plexiform layer; ONL, outer nuclear layer; VRI: Vitreoretinal interface.

mine the location of the band's posterior boundary. The plug-in offers the option to change the magnification of the B-scan where needed. No other modifications are possible before grading. To be judged as visible on the LRP, a clear peak or valley needs to be identifiable. In challenging cases, the reviewer is advised to refer to both the LRP and the B-scan. Small differences in reflectivity may be more apparent on the LRP and reveal bands that are difficult to distinguish on the B-scan. The B-scan allows for assessment of band visibility in adjacent regions, where the band in question may be more easily distinguishable. If any

retinal band did not fulfill these criteria for visibility, it was graded as “invisible” at this specific location, regardless of the underlying reason. After all locations are graded, the plug-in produces a .tsv (tab-separated values) output file. The Supplementary Material has a step-by-step explanation of the plug-in and an instructional Supplementary Video.

Study Populations

A group of 10 young adults, without ophthalmologic or systemic disease per self-report, were enrolled

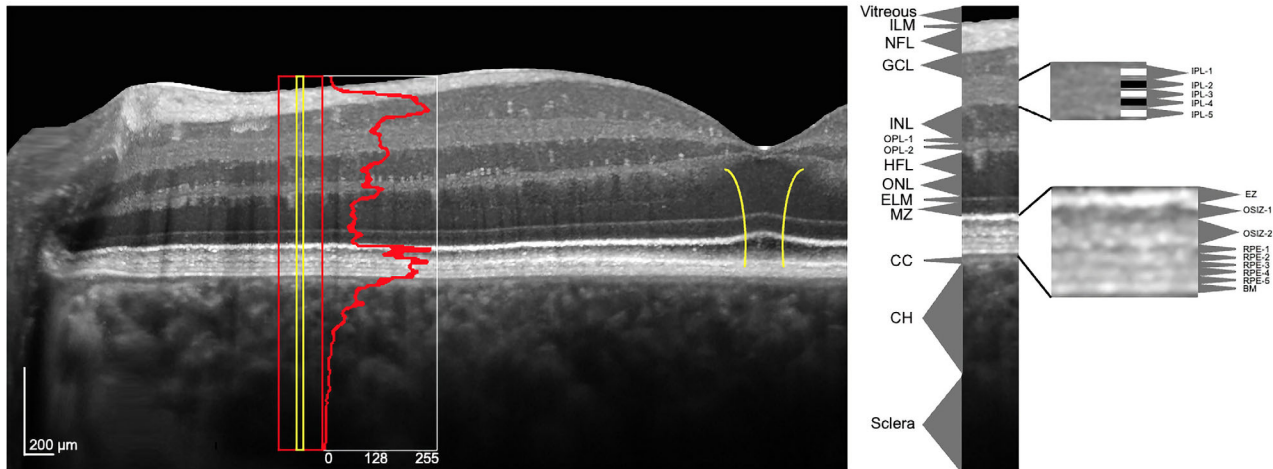


Figure 2. Presentation of the proposed high-resolution optical coherence tomography nomenclature in a healthy young eye. An exemplary representation of the proposed high-resolution optical coherence tomography nomenclature in the left eye of a 34-year-old healthy male, automated real-time averaging set to 100. The red frame is 20 A-scans wide ($\sim 200 \mu\text{m}$). The yellow lines within the red frame indicate the location of 3 A-scans used to compute the red longitudinal reflectivity profile. Reflectivity is measured as gray values [A.U.], in which 0 is black and 255 is white. Panels at right and far-right are magnified 150% and 200%, respectively. White and black rectangles show which IPL bands were graded as hyper- (white) and hypo- (black) reflective. Although the distinct retinal bands can be identified on the B-scan and even more so in the enlarged view, it is more difficult to do so by only relying on the LRP. The yellow lines at the foveal center highlight the location of the central bouquet, the area of highest density of cone photoreceptors and Müller cells. BM, Bruch membrane; CC, choriocapillaris; CH, choroid; GCL, ganglion cell layer; HFL, Henle fiber layer; IPL, inner plexiform layer; ILM, internal limiting membrane; MZ, myoid zone; NFL, nerve fiber layer; OPL, outer plexiform layer; ONL, outer nuclear layer.

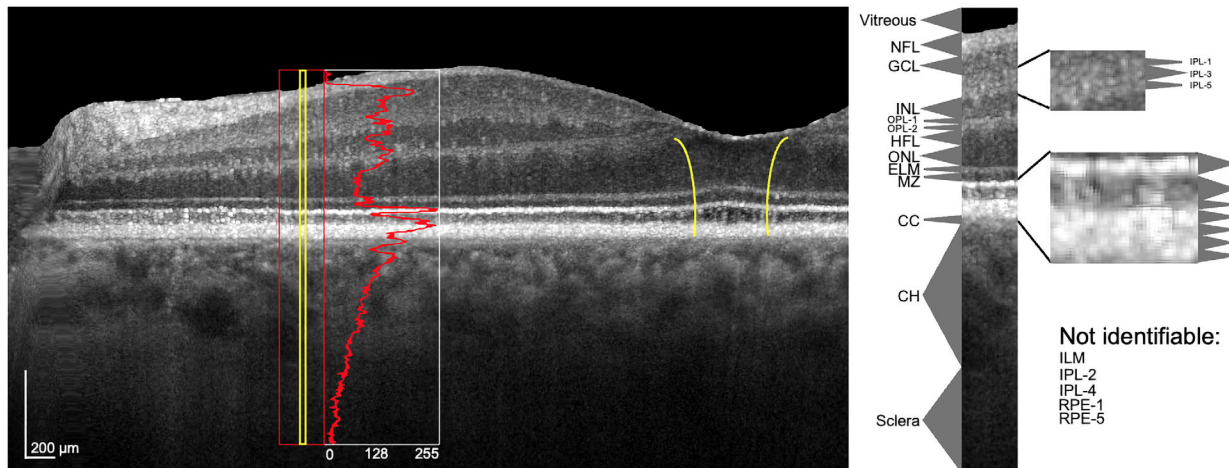


Figure 3. Presentation of the proposed high-resolution optical coherence tomography nomenclature in a healthy aged eye. An exemplary representation of the proposed high-resolution optical coherence tomography nomenclature in the left eye of a 65-year-old healthy female, automated real-time averaging set to 9. The red frame is 20 A-scans wide ($\sim 200 \mu\text{m}$). The yellow lines within the red frame indicate the location of three A-scans used to compute the red longitudinal reflectivity profile. Reflectivity is measured as gray values [A.U.], in which 0 is black and 255 is white. Panels at right and far-right are magnified 150% and 200%, respectively. Although the distinct retinal bands can be identified on the B-scan and even more so in the enlarged view, it is more difficult to do so by only relying on the LRP. Still, in this exemplary case, five bands were not identifiable (listed at bottom right corner). The yellow lines at the foveal center highlight the location of the central bouquet, the area of highest density of cone photoreceptors and Müller cells. Note that the yellow lines are oriented according to the external fovea (e.g., the rise of the ELM), which does not match the internal fovea (lowest point of the foveal depression), in this case. This common occurrence will be explored separately. BM, Bruch membrane; CC, choriocapillaris; CH, choroid; GCL, ganglion cell layer; HFL, Henle fiber layer; ILM, internal limiting membrane; IPL, inner plexiform layer; MZ, myoid zone; NFL, nerve fiber layer; OPL, outer plexiform layer; ONL, outer nuclear layer.

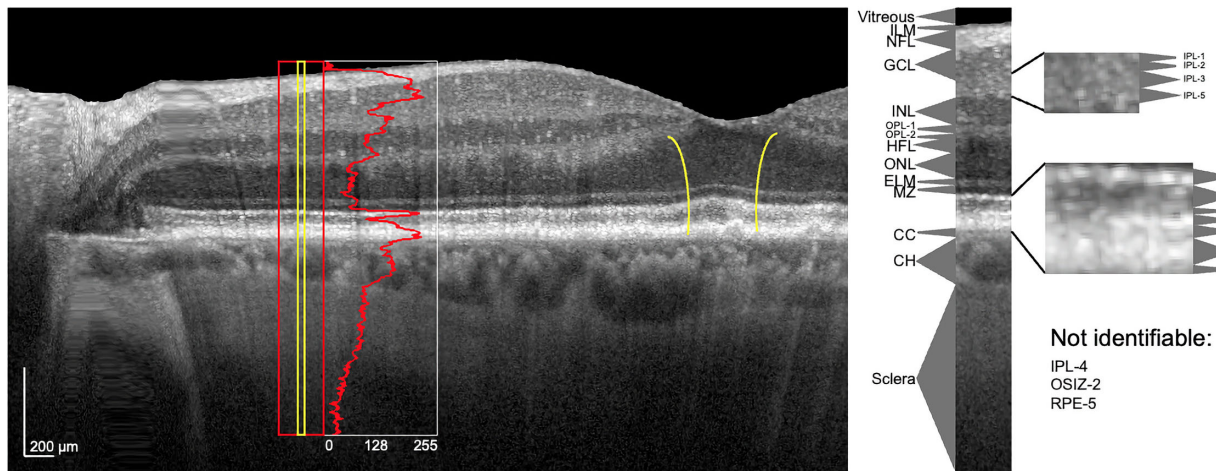


Figure 4. Presentation of the proposed high-resolution optical coherence tomography nomenclature in an eAMD eye. An exemplary representation of the proposed high-resolution optical coherence tomography nomenclature in the left eye of a 71-year-old female eAMD patient, automated real-time averaging set to 9. The inset is 20 A-scans wide ($\sim 200 \mu\text{m}$). The yellow lines within the red frame indicate the location of 3 A-scans used to compute the red longitudinal reflectivity profile. Reflectivity is measured as gray values [A.U.], in which 0 is black and 255 is white. While the distinct retinal bands can be identified on the B-scan and even more so in the enlarged view, it is more difficult to do so by only relying on the LRP. In this exemplary case, five bands were not identifiable (listed at bottom right corner). The yellow lines at the foveal center highlight the location of the central bouquet, the area of highest density of cone photoreceptors and Müller cells, as signified by the inward rise of the ELM. BM, Bruch membrane; CC, choriocapillaris; CH, choroid; GCL, ganglion cell layer; HFL, Henle fiber layer; IPL, inner plexiform layer; ILM, internal limiting membrane; MZ, myoid zone; NFL, nerve fiber layer; ONL, outer nuclear layer; OSIZ, outer segment interdigititation zone.

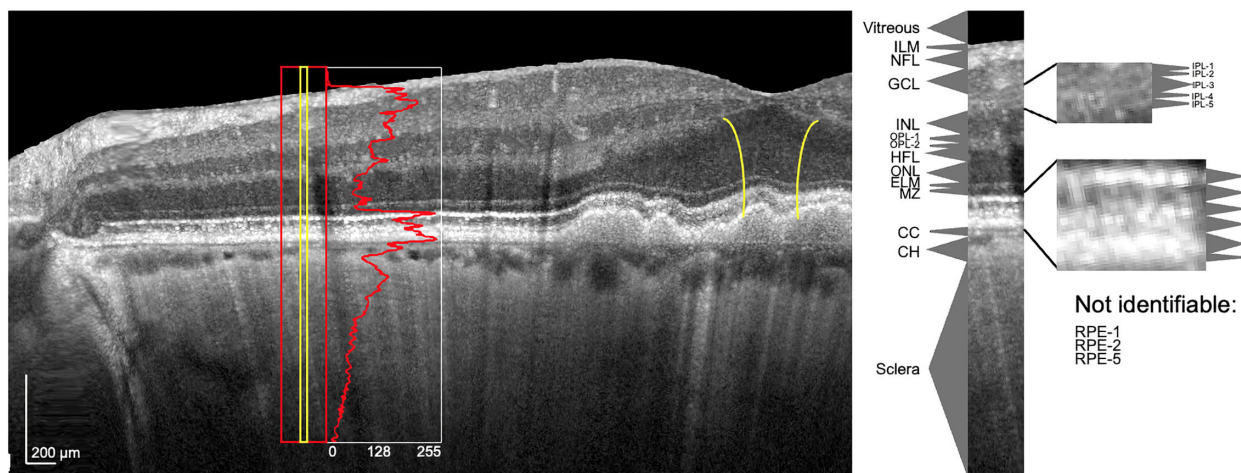


Figure 5. Presentation of the proposed High-Resolution Optical Coherence Tomography nomenclature in an iAMD eye. An exemplary representation of the proposed High-Resolution Optical Coherence Tomography nomenclature in the left eye of a 70-year-old male iAMD patient, automated real-time averaging set to 9. The red frame is 20 A-scans wide ($\sim 200 \mu\text{m}$). Panels at right and far-right are magnified 150% and 200%, respectively. The yellow lines within the red frame indicate the location of three A-scans used to compute the red longitudinal reflectivity profile. Reflectivity is measured as gray values [A.U.], in which 0 is black and 255 is white. Although the distinct retinal bands can be identified on the B-scan and even more so in the enlarged view, it is more difficult to do so by only relying on the LRP. In this exemplary case, five bands were not identifiable (listed at bottom right corner). The yellow lines at the foveal center highlight the location of the central bouquet, the area of highest density of cone photoreceptors and Müller cells. BM, Bruch membrane; CC, choriocapillaris; CH, choroid GCL, ganglion cell layer; HFL, Henle fiber layer; IPL, inner plexiform layer; ILM, internal limiting membrane; MZ, myoid zone; NFL, nerve fiber layer; ONL, outer nuclear layer; OPL, outer plexiform layer.

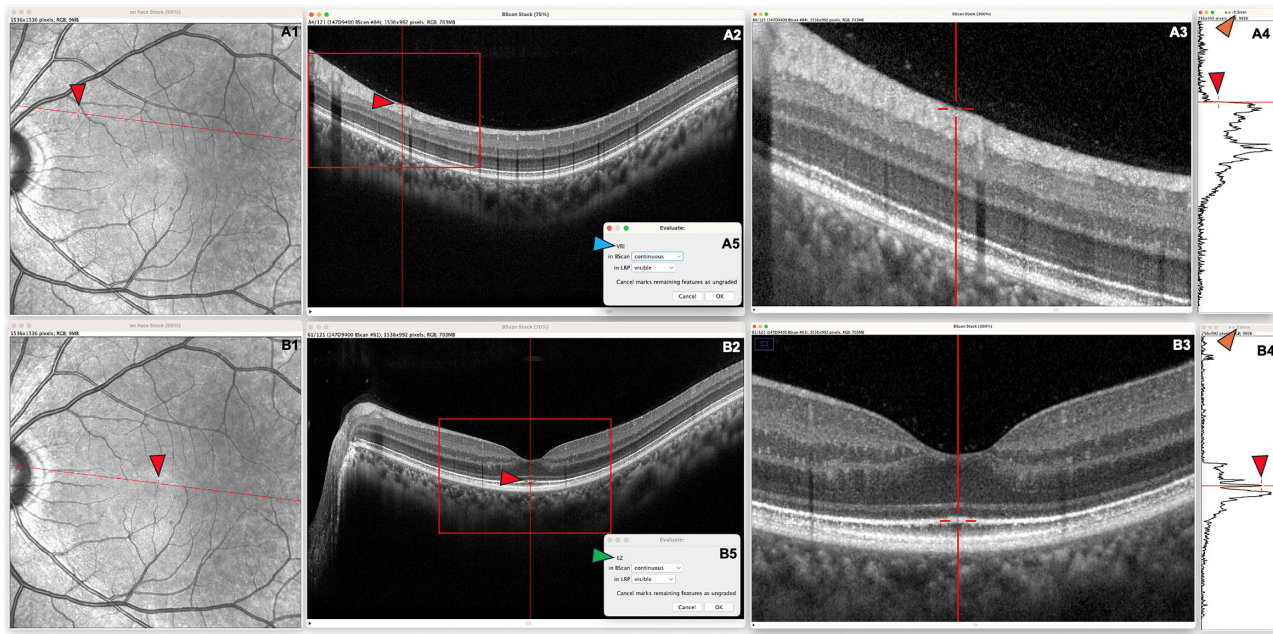


Figure 6. Step-by-Step guide through the custom ImageJ plug-in. Left eye of a 34-year-old male, ART 100. A1 – A5 show the first panels appearing after initiating the High-Res OCT review plug-in. A1 shows the IR localizer image. The red line indicates the position of the OCT B-scan at the 5° superior retina. A2 shows the OCT B-scan indicated in A1 at its original size. A3 is a magnified view (300%) of the inset in A2, which is the preferred grading magnification. A4 shows the longitudinal reflectivity profile of the respective grading location. A5 indicates the retinal boundary to be assessed (VRI, blue arrowhead) and allows for qualitative evaluation of retinal boundary visibility on the B-scan (A3, options: Continuous, discontinuous, not visible, not present, uncertain) and the longitudinal reflectivity profile (A4, options: Visible, split, not visible, not present). The orange arrowhead in A4 shows the grading location on the X-axis. Crosshairs in all images (red arrowheads) allow for a simultaneous assessment of a retinal location in the IR image, the OCT, and the LRP. To lock in the position of a boundary, the crosshair needs to be moved to the posterior boundary of the retinal band in question. Hitting “OK” in panel A5 saves the assessment for the respective horizontal and vertical position. After grading all retinal band boundaries in one location, the plug-in will move to the next location and the grading process will re-commence. B1–B5 show the same panels as A1–A5, although at the foveal center. The green arrowhead in B4 highlights the retinal band boundary in question. High-Res OCT, high-resolution optical coherence tomography; IR, infrared; VRI, vitreoretinal interface.

and imaged for a published study of OPL reflectivity.²¹ For this cohort, exclusion criteria were the presence of any confounding retinal conditions and high myopia (>6 diopters). A second group of adults (aged >70 years), with and without AMD, were recruited from the Callahan Eye Hospital Clinics at the University of Alabama at Birmingham. Patients with eAMD and iAMD using ICD-10 codes (H35.30*, H35.31*, H35.36*) were identified through EMR search. Each EMR was reviewed for eligibility (Author C.O.). Exclusion criteria included any confounding ocular conditions (e.g., glaucoma, diabetic retinopathy), neurological conditions (e.g., Alzheimer’s, cerebrovascular accidents), psychiatric disorders, diabetes, other impairing medical conditions, or terminal illnesses.⁶²

The study was approved by the Institutional Review Board of the University of Alabama at Birmingham. All participants provided written informed consent. This study adhered to tenets of the Declaration of Helsinki.

Retinal Imaging

Except for one young participant who was imaged in both eyes, all other young participants were imaged in one eye selected at random. Young participants underwent High-Res OCT imaging (Heidelberg Engineering, Heidelberg, Germany) in two paradigms (one foveal line scan at ART 100 and one OCT volume scan, 30° × 25°, 121 B-scans, ART 9, centered on the fovea). In aged participants, the eye with better BCVA was imaged after pupil dilation with 1% tropicamide and 2.5% phenylephrine hydrochloride. Aged adults also received color fundus photography (F450 Plus; Carl Zeiss Meditec, Jena, Germany) and High-Res OCT imaging (30° × 25°, 121 B-scans, ART 9, centered on the fovea). Photographs were used to assess AMD disease stages according to the AREDS 9-step classification system⁶³ by one experienced grader (Author M.E.C.) with good intragrader and intergrader reliability.⁶⁴ Healthy-aging was defined

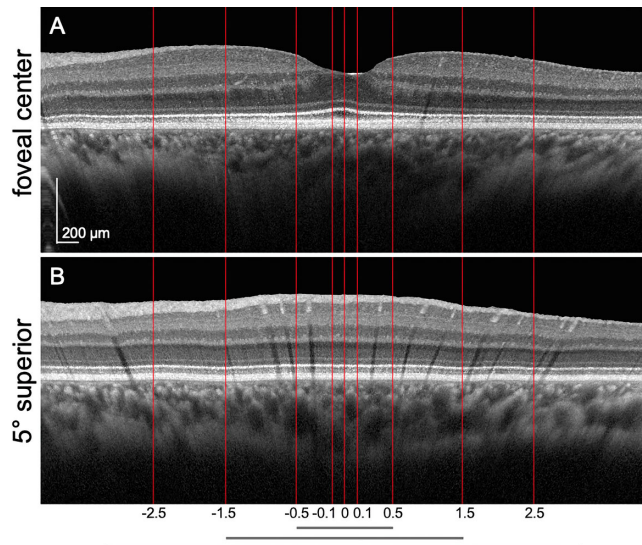


Figure 7. Distribution of the grading locations at 5° superior retina and fovea. Graphical presentation of the 9 grading locations at (A) the foveal center and (B) 5° superior retina in the left eye of a 31-year-old male, ART 100. The distance of the grading locations to the foveal center is shown in mm. The gray lines indicate the extent of the ETDRS central subfield (1 mm diameter), the inner ring (3 mm diameter), and the outer ring (6 mm diameter). To improve visibility, the OCT scan was straightened along Bruch membrane, consequently, hypertransmission trails appear non-axial.

as AREDS stage 1, eAMD as stages 2–4, and iAMD as stages 5–8.

Nomenclature Validation

We used five separate analyses to validate the proposed nomenclature with our long-term goals in mind. For all analyses, retinal band visibility was assessed on LRP and OCT B-scans by one grader (author L.G.). This grader has >7 years of Reading Center experience, including four as a senior grader. The .tsv files generated by the review software, including information about band discernibility at every graded location (example in the Supplementary Material), were used for further analyses. First, to analyze intrareader reliability, 10 eyes of 10 randomly selected participants (ART9, two healthy young, two healthy aged, three eAMD, three iAMD) were graded twice by the same reader several weeks apart.

Second, we graphically assessed visibility across all study eyes (ART9) using interlinked workbooks. Using spreadsheet software (Excel, Microsoft, Redmond WA, USA), the plug-in's output files ($n = 65$) were combined into one workbook with multiple tabs. For every band, visibility assessments were summed across tabs and divided by the total number of eyes in the respective diagnostic group. Visibility levels were color-coded

using the Conditional Formatting tool to highlight differences. Third, to investigate the impact of image averaging, we compared band visibility on the foveal B-scan in healthy young eyes, acquired with ART 9 and ART 100. Fourth, to investigate age-dependent differences in band visibility, we compared healthy young and healthy aged participants (ART9). Fifth, to investigate disease-related changes in band visibility, we compared healthy aged, eAMD, and iAMD participants (ART9).

Statistical Analysis

Continuous variables are presented as means and standard deviations (SD), Cohen's kappa was used to assess intrareader reliability. The χ^2 tests were used to compare retinal band visibilities in young healthy adults between ART 9 and ART 100 images. This analysis was done for individual gradings at each eccentricity. Furthermore, χ^2 tests were used to compare young healthy and healthy aged adults, and among healthy aged, eAMD, and iAMD participants. This analysis combined visibility across all eccentricities. Welch's analysis of variance was used to compare signal-to-noise ratios (expressed in dB per device output) between study groups.

Results

Cohort Characteristics

Table 1 presents cohort characteristics and images available for each study group. A total of 11 eyes of 10 healthy young adults (mean age 29.7 ± 3.6 years) and 54 eyes of 54 aged adults (mean age 76.2 ± 1.3 years) were included. Of these 54, 22 were graded as normal (mean age 74.6 ± 2.9 years), 17 as eAMD (77.7 ± 4.1 years), and 15 as iAMD (76.7 ± 4.7 years). Mean dB values reported by the Heyex software were 40 ± 4.1 , 35 ± 3.1 , 35 ± 3.9 , and 34 ± 4.3 for young, for healthy aged, eAMD, and iAMD eyes, respectively ($P < 0.01$, Welch's analysis of variance). Of note, these differences were not identifiable subjectively.

Nomenclature Validation

Intrareader Reliability

Intrareader reliability was moderate to near perfect. Cohen's κ ranged from 0.54–0.88 for the inner retinal bands. Intrareader reliability was poorest for IPL-2, IPL-3, and IPL-4 (Cohen's κ : 0.61, 0.54, 0.63, respectively) and best for the GCL (Cohen's κ : 0.88). For the

Table 1. Cohort Characteristics and Available High-Res OCT Data

	Young Adults	Healthy Aged	eAMD	iAMD
Cohort characteristics				
Patients (n)	10	22	17	15
Age [yr] \pm SD	29.7 \pm 3.6	74.6 \pm 2.9	77.7 \pm 4.1	76.7 \pm 4.7
Eyes (n)	11	22	17	15
Image quality [dB] \pm SD	40.0 \pm 4.1	35 \pm 3.2	35 \pm 3.9	34 \pm 4.3
Available High-Res OCT data				
25°x30°, 121 B-scans, ART 9	Yes	Yes	Yes	Yes
Foveal B-scan, ART 100	Yes	No	No	No

ART, automated real-time averaging; dB, decibel; eAMD, early age-related macular degeneration; High-Res OCT, High-Resolution Optical Coherence Tomography; iAMD, intermediate age-related macular degeneration; SD, standard deviation; yr, years.

outer retinal bands Cohen's κ ranged 0.67–0.83. The intrareader reliability was lowest for RPE-2, RPE-3, RPE-5, and OSIZ-2 (Cohen's κ : 0.67, 0.69, 0.68, 0.71, respectively) and best for the EZ (Cohen's κ : 0.83).

Retinal Band Visibility Across All Eyes

Results of statistical tests for visibility are shown in Tables 2–5. Tables 2A, 2B display results for healthy young eyes, as graded on ART 9 images at 5° superior retina (Table 2A) and the foveal center (Table 2B). It is noteworthy that RPE-2 and RPE-3 were hardly visible along the B-scan at the foveal center, while they were reliably seen through the B-scan at 5° superior retina. Tables 3A, 3B show the results for healthy aged eyes. Comparing healthy aged to healthy young eyes, the RPE bands are less discernable at both retinal locations. Tables 4A and 4B show the results for eAMD eyes. Visibility of the outer retinal bands was similar compared to healthy aged eyes. Tables 5A and 5B show the results for iAMD eyes, in which the difficulties in band discernibility also include the RPE bands and OSIZ-1 and OSIZ-2.

We investigated ELM and EZ visibility in all eyes as these were used to define the foveal center. Both bands were identifiable in all but seven eyes. Three eyes of these seven were graded as normal and four as iAMD. Underlying pathologies were subretinal drusenoid deposit, drusen, and incomplete outer retinal atrophy.

Comparison Between ART9 and ART100

Table 6 compares band visibility in ART 9 and ART 100 images captured from healthy young adults (n = 11 eyes). IPL-4 was visible in four cases in ART9 images and in nine cases in ART100 ($P = 0.03$). OPL-2 was visible in five cases in ART9, compared to eleven cases in ART100 ($P = 0.02$).

All other retinal bands did not differ significantly between ART9 and ART100, showing moderate (>6 cases for all other bands in ART9) and good visibility (>8 in ART100) in the respective image acquisition modes.

Age-Dependent Differences in Retinal Band Visibility

Table 7 compares band visibility between healthy young (n = 10) and healthy aged adults (n = 22, middle column). One eye from a young person with two tested eyes was excluded to avoid biases in statistical analysis. IPL-2 is significantly less visible in healthy aged, compared to healthy young eyes ($P = 0.02$). Similarly, OSIZ-2 and RPE-1 are much less visible in healthy aged eyes ($P = 0.01$ for both comparisons). In addition, RPE-2, -3, and -5 were less frequently visible in healthy aged compared to healthy young eyes ($P < 0.001$, $P < 0.001$, and $P = 0.02$, respectively). The other retinal bands revealed good and similar visibility in both cohorts.

Disease-Dependent Differences in Retinal Band Visibility

Table 7 shows the results comparing healthy aged (n = 22), eAMD (n = 17), and iAMD (n = 15, right column) eyes. The OSIZ-1 is easily visible in healthy aged eyes, and less so in eAMD and iAMD eyes ($P = 0.02$). The OSIZ-2 is well visible in healthy aged and eAMD eyes and less visible in iAMD eyes ($P < 0.0001$). Similar relations can be observed regarding RPE-2. However, band visibility is already impaired in healthy aging, which becomes more apparent in eAMD and iAMD (<0.001). RPE-5 is difficult to identify in healthy aging and eAMD but is more apparent in iAMD ($P < 0.001$). No significant differences were identified for any other retinal band. RPE-2 and RPE-3

Table 2A. Percent Retinal Band Visibility in Healthy Young Eyes (n = 10) at 5° Superior Retina

	5° superior retina									
X(mm)	-2.5	-1.5	-0.5	-0.1	0.0	0.1	0.5	1.5	2.5	
Y(mm)	1.4	1.4	1.4	1.4	1.4	1.4	1.4	1.4	1.4	
VRI	100	100	100	100	100	100	100	100	100	
ILM	80	80	60	80	70	90	90	80	80	
NFL	100	100	100	100	100	100	100	100	100	
GCL	100	100	100	100	100	100	100	100	100	
IPL-1	100	100	100	100	100	100	100	100	100	
IPL-2	90	100	100	100	100	90	100	100	100	
IPL-3	80	90	100	100	90	100	100	100	100	
IPL-4	80	80	90	100	70	90	90	100	100	
IPL-5	100	100	100	100	100	100	100	100	100	
INL	100	100	100	100	100	100	100	100	100	
OPL-1	100	100	100	100	100	100	100	100	100	
OPL-2	100	100	100	100	100	100	100	100	80	
HFL	70	90	90	90	100	90	90	100	90	
ONL	100	100	100	100	100	100	100	100	100	
ELM	100	100	100	100	100	100	100	100	100	
MZ	100	100	100	100	100	100	100	100	100	
EZ	100	100	100	100	100	100	100	100	100	
OSIZ-1	100	100	100	100	100	100	100	100	100	
OSIZ-2	90	100	100	90	100	90	90	100	100	
RPE-1	90	80	90	80	100	90	80	90	100	
RPE-2	100	80	80	80	80	80	70	80	90	
RPE-3	80	70	80	70	60	70	60	50	70	
RPE-4	100	100	100	100	100	100	100	100	100	
RPE-5	80	50	50	30	40	40	30	70	40	
BM	100	100	100	100	100	100	100	100	100	
CC	100	100	100	100	100	100	100	100	100	
CH	100	100	100	100	100	90	90	90	90	

X: location on the X-axis, Y: location on the Y-axis, VRI: Vitreoretinal interface, ILM: Internal limiting membrane, NFL: Nerve fiber layer, GCL: Ganglion-cell layer, IPL: Inner plexiform layer, INL: Inner nuclear layer, OPL: Outer plexiform layer, HFL: Henle fiber layer, ONL: Outer nuclear layer, ELM: External limiting membrane, MZ: Myoid zone, EZ: Ellipsoid Zone, OSIZ: Outer segment interdigitation zone, RPE: Retinal pigment epithelium, BM: Bruch membrane, CC: Choriocapillaris, CH: Choroid, Visibility levels were highlighted using the Conditional Formatting tool. Green with white font: 100% visibility. Green: $\geq 75\%$ visibility, yellow: $\geq 50 - < 75\%$ visibility, red: $< 50\%$ visibility.

were not easily identifiable, which was consistent across all study groups.

Discussion

To create a $<3\ \mu\text{m}$ OCT review tool for ImageJ, we incorporated into the most recent consensus nomenclature²⁰ recent advances in histology, electron microscopy, and experimental OCT devices.^{21–24} Compared to existing nomenclature, the added bands are IPL-1-5, OPL-1-2, OSIZ-1-2, and RPE-1-5. Our novel review tool facilitates accurate and standardized assessment of retinal band visibility

Table 2B. Percent Retinal Band Visibility in Healthy Young Eyes (n = 10) at the Foveal B-Scan

	Fovea									
X (mm)	-2.5	-1.5	-0.5	-0.1	0.0	0.1	0.5	1.5	2.5	
Y (mm)	0.0	0.0	0.0	0.0	0.0	0.0	0.0	0.0	0.0	
VRI	100	100	100	100	90	100	100	100	100	
ILM	60	80	80	100	100	100	80	90	80	
NFL	100	100	80	0	0	10	50	100	100	
GCL	100	100	100	10	0	20	100	100	100	
IPL-1	100	100	70	10	0	10	50	100	100	
IPL-2	90	90	50	10	0	10	30	100	100	
IPL-3	90	100	20	0	0	0	60	100	100	
IPL-4	80	90	40	0	0	0	50	80	90	
IPL-5	100	100	90	0	0	10	100	100	100	
INL	100	100	100	20	0	10	100	100	100	
OPL-1	100	100	100	20	0	10	100	100	90	
OPL-2	100	100	80	0	0	0	100	100	100	
HFL	100	100	100	100	100	100	100	100	100	
ONL	100	100	100	100	100	100	100	100	100	
ELM	100	100	100	100	100	100	100	100	100	
MZ	100	100	100	100	100	100	100	100	100	
EZ	100	100	100	100	100	100	100	100	100	
OSIZ-1	100	100	100	100	100	100	100	100	100	
OSIZ-2	100	90	100	100	100	100	100	100	100	
RPE-1	90	90	80	90	70	80	90	80	80	
RPE-2	70	60	0	0	0	10	0	50	90	
RPE-3	60	40	0	0	0	10	0	40	80	
RPE-4	100	100	100	100	100	100	100	100	100	
RPE-5	90	80	30	60	60	50	50	30	70	
BM	100	100	100	100	100	100	100	100	100	
CC	100	100	100	100	100	100	100	100	100	
CH	90	90	90	90	90	90	90	90	90	

X: location on the X-axis, Y: location on the Y-axis, VRI: Vitreoretinal interface, ILM: Internal limiting membrane, NFL: Nerve fiber layer, GCL: Ganglion-cell layer, IPL: Inner plexiform layer, INL: Inner nuclear layer, OPL: Outer plexiform layer, HFL: Henle fiber layer, ONL: Outer nuclear layer, ELM: External limiting membrane, MZ: Myoid zone, EZ: Ellipsoid Zone, OSIZ: Outer segment interdigitation zone, RPE: Retinal pigment epithelium, BM: Bruch membrane, CC: Choriocapillaris, CH: Choroid, Visibility levels were highlighted using the Conditional Formatting tool. Green with white font: 100% visibility. Green: $\geq 75\%$ visibility, yellow: $\geq 50 - < 75\%$ visibility, red: $< 50\%$ visibility.

and posterior boundary location. Commonly used OCT review software is designed for decisions about retinal thickness and anti-VEGF treatment in daily clinical practice. Because this software requires approval by regulatory authorities, modification for research questions cannot easily be implemented. ImageJ was initially developed for analyzing multi-scale microscopy images⁵⁹ and can be readily adapted for clinical images. We found that the visibility of retinal bands comprised in our refined nomenclature was identifiable using a novel review tool. The tool also captured differences in retinal anatomy between young and healthy aged adults and between healthy aged, eAMD, and iAMD eyes. We discuss supporting microscopy and prototype imaging data, band visibility, and implications for algorithm training for automation.

Table 3A. Percent Retinal Band Visibility in Healthy Aged Eyes (n = 22) at 5° Superior Retina

5° superior retina									
X(mm)	-2.5	-1.5	-0.5	-0.1	0.0	0.1	0.5	1.5	2.5
Y(mm)	1.4	1.4	1.4	1.4	1.4	1.4	1.4	1.4	1.4
VRI	95	95	95	95	95	95	95	95	95
ILM	77	82	73	82	82	86	86	86	86
NFL	91	91	91	91	91	91	91	86	86
GCL	82	91	91	91	91	86	91	86	86
IPL-1	77	86	86	86	82	86	82	86	86
IPL-2	59	77	73	86	82	86	77	82	77
IPL-3	77	86	82	91	86	91	86	82	68
IPL-4	68	82	86	86	82	86	82	82	68
IPL-5	86	91	91	91	91	91	91	91	91
INL	91	91	91	91	91	91	91	91	91
OPL-1	91	91	91	91	91	91	91	91	91
OPL-2	82	77	82	91	86	91	91	91	82
HFL	27	68	82	91	86	82	82	77	55
ONL	91	91	91	91	91	91	91	91	91
ELM	91	91	91	91	91	91	91	91	91
MZ	91	91	91	91	91	91	91	91	91
EZ	91	91	91	91	91	91	91	91	91
OSIZ-1	86	91	91	91	91	91	91	91	91
OSIZ-2	77	77	73	73	77	73	77	82	86
RPE-1	64	59	50	68	64	64	64	64	68
RPE-2	36	32	9	9	5	9	14	36	41
RPE-3	41	27	5	5	9	5	14	36	41
RPE-4	91	86	91	91	91	91	91	91	91
RPE-5	36	41	18	18	9	27	18	9	23
BM	91	91	91	91	91	91	91	91	91
CC	91	91	91	91	91	91	91	91	91
CH	91	91	91	91	91	91	91	91	91

X: location on the X-axis, Y: location on the Y-axis, VRI: Vitreoretinal interface, ILM: Internal limiting membrane, NFL: Nerve fiber layer, GCL: Ganglion-cell layer, IPL: Inner plexiform layer, INL: Inner nuclear layer, OPL: Outer plexiform layer, HFL: Henle fiber layer, ONL: Outer nuclear layer, ELM: External limiting membrane, MZ: Myoid zone, EZ: Ellipsoid Zone, OSIZ: Outer segment interdigitation zone, RPE: Retinal pigment epithelium, BM: Bruch membrane, CC: Choriocapillaris, CH: Choroid, Visibility levels were highlighted using the Conditional Formatting tool. Green with white font: 100% visibility. Green: $\geq 75\%$ visibility, yellow: $\geq 50 - < 75\%$ visibility, red: $< 50\%$ visibility.

Microscopy Data To Inform OCT Nomenclature

Inner Retina

The 5-layered IPL formalizes observations from fundamental neuroscience research over decades and represents the cellular basis of parallel visual pathways from retina to brain.⁴⁶ IPL lamination has been previously seen via SD-OCT using a broadband light source,⁴⁷ and experimental devices (vis-OCT, and near-infrared-OCT, axial resolution 1.4 μm ⁶⁵ and 4.2 μm ⁶⁶ respectively). In our results, the five sub-bands were slightly less reliable than other inner retinal bands (94% visible vs 100%). For internal consistency in our software, our IPL numbering system (inner to outer) is

Table 3B. Percent Retinal Band Visibility in Healthy Aged Eyes (n = 22) at the Foveal B-Scan

Fovea									
X (mm)	-2.5	-1.5	-0.5	-0.1	0.0	0.1	0.5	1.5	2.5
Y (mm)	0.0	0.0	0.0	0.0	0.0	0.0	0.0	0.0	0.0
VRI	95	95	95	95	95	95	95	95	95
ILM	86	77	41	91	91	91	45	91	82
NFL	91	91	86	0	0	0	77	86	91
GCL	91	91	91	9	0	0	91	86	91
IPL-1	82	86	68	9	0	5	77	86	86
IPL-2	82	82	36	0	0	0	36	82	82
IPL-3	82	86	41	0	0	0	32	77	82
IPL-4	86	86	18	0	0	5	5	64	82
IPL-5	91	91	77	5	0	0	73	91	91
INL	91	91	91	9	0	0	91	91	91
OPL-1	86	91	91	14	0	0	91	91	91
OPL-2	82	91	45	5	0	0	64	91	91
HFL	68	91	91	82	91	91	91	91	91
ONL	91	91	91	91	91	91	91	91	91
ELM	91	91	91	91	91	91	91	91	91
MZ	91	91	91	91	91	91	91	91	91
EZ	91	91	91	91	86	91	91	91	91
OSIZ-1	91	86	82	91	86	91	91	91	86
OSIZ-2	77	77	59	50	45	45	68	86	77
RPE-1	59	68	50	36	36	41	55	73	68
RPE-2	36	18	5	5	5	5	5	14	50
RPE-3	27	18	9	5	5	5	5	9	45
RPE-4	91	91	91	91	91	91	86	91	91
RPE-5	41	23	14	32	41	27	23	5	14
BM	91	91	91	86	91	91	91	91	91
CC	91	91	91	91	91	91	91	91	91
CH	91	91	91	91	91	91	91	91	91

X: location on the X-axis, Y: location on the Y-axis, VRI: Vitreoretinal interface, ILM: Internal limiting membrane, NFL: Nerve fiber layer, GCL: Ganglion-cell layer, IPL: Inner plexiform layer, INL: Inner nuclear layer, OPL: Outer plexiform layer, HFL: Henle fiber layer, ONL: Outer nuclear layer, ELM: External limiting membrane, MZ: Myoid zone, EZ: Ellipsoid Zone, OSIZ: Outer segment interdigitation zone, RPE: Retinal pigment epithelium, BM: Bruch membrane, CC: Choriocapillaris, CH: Choroid, Visibility levels were highlighted using the Conditional Formatting tool. Green with white font: 100% visibility. Green: $\geq 75\%$ visibility, yellow: $\geq 50 - < 75\%$ visibility, red: $< 50\%$ visibility.

opposite to that of Ghassabi et al.,²⁴ which follows a long-standing neuroscience precedence to order layers in the direction of information transmission. The five-layered IPL captures a top-level division in visual signal processing as to whether ganglion cells respond when a light comes ON or OFF within a receptive field.^{67,68} Defined morphologic phenotypes of ON ganglion cells axons ramify strictly in the inner IPL (IPL-1,2,3 in our scheme), whereas OFF ganglion cell axons ramify strictly in the outer IPL (IPL-4,5). Rod bipolar cells, of one morphologic type, are all ON and terminate in OCT IPL-1. Cone bipolar cells (12 known types) can be classified into either OFF or ON, with ON terminating in either OCT IPL-2 or -3 and OFF terminating in either IPL-4 or -5. Each cell type is molecularly distinct, with specific synaptic endings forming the sublayers, as demonstrated with multiplex immunohistochemistry^{45,46} and correlated to reflectivity bands in broad-

Table 4A. Percent Retinal Band Visibility in eAMD eyes (n = 17) at 5° Superior Retina

	5° superior retina									
X(mm)	-2.5	-1.5	-0.5	-0.1	0.0	0.1	0.5	1.5	2.5	
Y(mm)	1.4	1.4	1.4	1.4	1.4	1.4	1.4	1.4	1.4	
VRI	100	100	100	100	100	100	100	100	100	
ILM	94	94	76	88	82	82	94	94	94	
NFL	100	100	100	100	100	100	100	100	100	
GCL	100	100	94	94	94	100	100	100	94	
IPL-1	100	88	88	94	94	94	100	100	94	
IPL-2	100	88	94	94	94	88	88	94	88	
IPL-3	100	88	100	94	94	94	88	88	82	
IPL-4	100	94	94	88	94	88	76	88	82	
IPL-5	100	100	100	94	100	100	100	100	94	
INL	100	100	100	100	100	100	100	100	100	
OPL-1	100	100	100	100	100	100	100	100	100	
OPL-2	94	94	100	100	100	100	100	100	88	
HFL	65	82	88	88	100	94	94	94	65	
ONL	100	100	100	100	100	100	100	100	100	
ELM	100	100	100	100	100	100	100	100	100	
MZ	100	100	100	100	100	100	100	100	100	
EZ	100	100	100	100	100	100	100	100	100	
OSIZ-1	100	100	100	100	100	100	94	94		
OSIZ-2	94	100	100	100	100	100	88	88	100	
RPE-1	94	100	82	71	82	94	65	76	76	
RPE-2	47	35	12	12	12	6	6	18	41	
RPE-3	29	24	6	6	6	0	6	12	29	
RPE-4	100	100	100	100	100	100	100	100	100	
RPE-5	59	29	47	29	53	71	41	59	29	
BM	100	100	100	100	100	100	100	100	100	
CC	100	100	100	100	100	100	100	100	100	
CH	100	100	100	100	100	100	100	100	100	

X: location on the X-axis, Y: location on the Y-axis, VRI: Vitreoretinal interface, ILM: Internal limiting membrane, NFL: Nerve fiber layer, GCL: Ganglion-cell layer, IPL: Inner plexiform layer, INL: Inner nuclear layer, OPL: Outer plexiform layer, HFL: Henle fiber layer, ONL: Outer nuclear layer, ELM: External limiting membrane, MZ: Myoid zone, EZ: Ellipsoid Zone, OSIZ: Outer segment interdigitation zone, RPE: Retinal pigment epithelium, BM: Bruch membrane, CC: Choriocapillaris, CH: Choroid, Visibility levels were highlighted using the Conditional Formatting tool. Green with white font: 100% visibility. Green: $\geq 75\%$ visibility, yellow: $\geq 50 - < 75\%$ visibility, red: $< 50\%$ visibility.

band SDOCT by Tanna et al.⁴⁷ (their Fig. 3). Müller glia and microglia ramify in these sublayers too and are likely to contribute reflectivity. We acknowledge that the visibility of IPL sub bands may be distorted focally by large vessels, superficial vessels, and to a lesser degree, connecting capillaries of the superficial and intermediate capillary plexuses. In a coming era of oculomics,⁶⁹ (i.e., using the retina to monitor other organ systems), one can imagine that neurodegenerations may be particularly visible in the five-banded IPL of $< 3\text{ }\mu\text{m}$ OCT.

Histologic Validation of Outer Retinal OCT: Challenges and Solutions

Regarding the outer retina, challenges to histologic validation of signal sources for reflective bands

Table 4B. Percent Retinal Band Visibility in eAMD (n = 17) at the Foveal B-Scan

	Fovea									
X (mm)	-2.5	-1.5	-0.5	-0.1	0.0	0.1	0.5	1.5	2.5	
Y (mm)	0.0	0.0	0.0	0.0	0.0	0.0	0.0	0.0	0.0	
VRI	100	100	100	100	100	100	100	100	100	
ILM	82	88	65	100	100	100	100	71	100	
NFL	100	100	88	0	6	0	76	94	94	
GCL	100	100	100	24	12	12	100	100	94	
IPL-1	100	100	82	18	6	18	82	100	94	
IPL-2	88	94	41	6	0	0	29	88	88	
IPL-3	94	82	53	6	0	0	35	88	94	
IPL-4	88	82	35	0	0	0	24	82	82	
IPL-5	100	100	88	6	6	0	94	100	100	
INL	100	100	100	24	12	12	100	100	100	
OPL-1	100	100	100	24	12	12	100	100	100	
OPL-2	94	94	47	0	0	0	59	100	100	
HFL	88	100	100	94	100	100	100	100	94	
ONL	100	100	100	100	100	100	100	100	100	
ELM	100	100	100	100	100	100	100	100	100	
MZ	100	100	100	100	100	100	100	100	100	
EZ	100	100	100	100	100	100	100	100	100	
OSIZ-1	100	100	100	100	100	100	100	100	94	
OSIZ-2	94	88	76	88	76	71	88	76	82	
RPE-1	53	71	65	47	59	59	47	71	82	
RPE-2	29	12	6	0	0	0	0	6	35	
RPE-3	24	12	0	0	0	0	0	12	24	
RPE-4	100	94	100	100	94	100	100	100	100	
RPE-5	59	53	53	59	71	71	53	18	18	
BM	100	100	100	100	100	100	100	100	100	
CC	100	100	100	100	100	100	100	100	100	
CH	100	100	100	100	100	100	100	100	100	

X: location on the X-axis, Y: location on the Y-axis, VRI: Vitreoretinal interface, ILM: Internal limiting membrane, NFL: Nerve fiber layer, GCL: Ganglion-cell layer, IPL: Inner plexiform layer, INL: Inner nuclear layer, OPL: Outer plexiform layer, HFL: Henle fiber layer, ONL: Outer nuclear layer, ELM: External limiting membrane, MZ: Myoid zone, EZ: Ellipsoid Zone, OSIZ: Outer segment interdigitation zone, RPE: Retinal pigment epithelium, BM: Bruch membrane, CC: Choriocapillaris, CH: Choroid, Visibility levels were highlighted using the Conditional Formatting tool. Green with white font: 100% visibility. Green: $\geq 75\%$ visibility, yellow: $\geq 50 - < 75\%$ visibility, red: $< 50\%$ visibility.

(Supplementary Table S1) have driven technologic advances like $< 3\text{ }\mu\text{m}$ OCT. The horizontally aligned, vertically oriented outer retinal cells increase axial resolution beyond that shown in the LRP (Fig. 2), because an observer can integrate information at either side of any one test location. Specific challenges include numerous distinct layers, the clinical utility of multi-scale information (organelle, cell, layer, regional), small cross-sectional diameters of photoreceptor IS and OS, and detachment and compaction (bending) artifacts involving photoreceptor OS and RPE apical processes. To assist in interpreting the histology literature and motivate future innovation, many known tissue, microscopy, illustrative, and interpretive artifacts are listed in Supplementary Table S1.

One solution for validating outer retinal OCT in normal eyes is volume EM, providing multiple aligned EM images at nanometer scale. In rapidly preserved organ donor eyes, with minimal detachments

Table 5A. Percent Retinal Band Visibility in iAMD Eyes (n = 15) at 5° Superior Retina

	5° superior retina									
X(mm)	-2.5	-1.5	-0.5	-0.1	0.0	0.1	0.5	1.5	2.5	
Y(mm)	1.4	1.4	1.4	1.4	1.4	1.4	1.4	1.4	1.4	1.4
VRI	100	100	100	100	100	100	100	100	100	100
ILM	100	100	93	93	93	93	100	93	100	
NFL	100	100	100	100	100	100	100	100	100	
GCL	100	100	100	100	100	100	100	100	73	
IPL-1	100	100	100	100	100	93	100	100	87	
IPL-2	100	100	100	100	93	87	93	93	80	
IPL-3	87	93	100	93	87	80	87	93	80	
IPL-4	87	80	93	87	80	80	80	87	80	
IPL-5	100	100	100	100	100	100	100	100	100	
INL	100	100	100	100	100	100	100	100	100	
OPL-1	100	100	100	100	100	100	100	100	93	
OPL-2	93	87	100	93	87	100	93	93	93	
HFL	27	80	87	87	100	87	80	73	67	
ONL	100	100	100	100	100	100	100	100	100	
ELM	100	100	100	100	100	100	100	100	100	
MZ	100	100	100	100	100	100	100	93	100	
EZ	93	100	100	100	100	100	93	100		
OSIZ-1	93	93	87	87	93	100	87	80	87	
OSIZ-2	53	47	60	47	47	53	47	47	67	
RPE-1	53	47	47	27	33	40	33	47	60	
RPE-2	27	13	13	20	27	20	27	33	47	
RPE-3	20	7	7	7	13	7	13	20	40	
RPE-4	93	93	87	93	93	93	93	93	93	
RPE-5	40	53	53	40	47	53	60	60	27	
BM	93	93	100	93	93	93	93	93	93	
CC	100	93	93	93	93	100	93	93	100	
CH	100	100	100	100	100	100	100	100	100	

X: location on the X-axis, Y: location on the Y-axis, VRI: Vitreoretinal interface, ILM: Internal limiting membrane, NFL: Nerve fiber layer, GCL: Ganglion-cell layer, IPL: Inner plexiform layer, INL: Inner nuclear layer, OPL: Outer plexiform layer, HFL: Henle fiber layer, ONL: Outer nuclear layer, ELM: External limiting membrane, MZ: Myoid zone, EZ: Ellipsoid Zone, OSIZ: Outer segment interdigitation zone, RPE: Retinal pigment epithelium, BM: Bruch membrane, CC: Choriocapillaris, CH: Choroid, Visibility levels were highlighted using the Conditional Formatting tool. Green with white font: 100% visibility. Visibility levels were highlighted using the Conditional Formatting tool. Green with white font: 100% visibility. Green: $\geq 75\%$ visibility, yellow: $\geq 50 - < 75\%$ visibility, red: $< 50\%$ visibility.

yet still subject to compactations, the resulting images are high-resolution, high magnification, comprehensive (all pixels accounted for), unbiased, and multi-scale. A solution for diseased eyes is clinicopathologic correlation (i.e., histology of eyes imaged with OCT during life). Thus perturbed reflective bands serve as strong independent variables and can contextualize histology of donor eyes lacking ophthalmic history. We prioritize these approaches in this next section.

Outer Retina—Well-Supported Bands

In the current study, the OPL was divided into an inner band of homogeneous moderate reflectivity distinct from individual vessels of the deep capillary plexus and an outer thinner band of higher reflectivity. An intervening hyporeflective band was rarely

Table 5B. Percent Retinal Band Visibility in iAMD (n = 15) at the Foveal B-Scan

	Fovea									
X (mm)	-2.5	-1.5	-0.5	-0.1	0.0	0.1	0.5	1.5	2.5	
Y (mm)	0.0	0.0	0.0	0.0	0.0	0.0	0.0	0.0	0.0	0.0
VRI	100	100	100	100	100	100	100	100	100	100
ILM	100	93	67	100	100	100	100	67	100	93
NFL	100	100	93	0	0	0	0	73	100	100
GCL	100	100	100	13	7	13	100	100	93	93
IPL-1	93	93	87	13	7	13	100	93	93	93
IPL-2	73	93	73	0	0	0	73	93	93	93
IPL-3	73	87	47	0	0	0	47	80	93	93
IPL-4	73	73	40	0	0	0	40	80	80	80
IPL-5	100	100	93	0	0	7	93	100	100	100
INL	100	100	100	13	7	13	100	100	100	100
OPL-1	100	100	100	13	7	13	100	100	100	100
OPL-2	80	100	53	0	0	0	47	93	93	93
HFL	87	100	100	100	100	100	100	100	100	87
ONL	100	100	100	100	100	100	100	100	100	100
ELM	100	100	100	93	100	100	100	100	100	100
MZ	100	100	100	100	100	100	100	100	100	100
EZ	100	100	100	87	87	93	93	100	100	100
OSIZ-1	93	93	93	93	87	80	93	87	87	87
OSIZ-2	73	60	33	40	20	20	27	67	60	60
RPE-1	53	47	27	27	20	13	13	73	40	40
RPE-2	20	27	7	7	13	7	13	13	33	33
RPE-3	7	7	0	0	7	0	7	7	27	27
RPE-4	87	93	93	93	93	93	93	87	93	93
RPE-5	53	47	53	73	73	80	53	53	33	33
BM	93	93	93	93	93	93	93	93	93	93
CC	87	87	100	93	93	93	93	93	93	93
CH	100	100	100	93	100	100	100	100	100	100

X: location on the X-axis, Y: location on the Y-axis, VRI: Vitreoretinal interface, ILM: Internal limiting membrane, NFL: Nerve fiber layer, GCL: Ganglion-cell layer, IPL: Inner plexiform layer, INL: Inner nuclear layer, OPL: Outer plexiform layer, HFL: Henle fiber layer, ONL: Outer nuclear layer, ELM: External limiting membrane, MZ: Myoid zone, EZ: Ellipsoid Zone, OSIZ: Outer segment interdigitation zone, RPE: Retinal pigment epithelium, BM: Bruch membrane, CC: Choriocapillaris, CH: Choroid, Green with white font: 100% visibility. Visibility levels were highlighted using the Conditional Formatting tool. Green with white font: 100% visibility. Green: $\geq 75\%$ visibility, yellow: $\geq 50 - < 75\%$ visibility, red: $< 50\%$ visibility.

seen, thus prompting our suggestions of OPL1-2. HR-OCT images of young adults from the current study were recently compared to volume electron microscopy of OPL in an age-similar organ-donor retina.²¹ Mitochondria were quantified because of their known role in reflectivity (see next paragraph). The peak-to-peak separation between two hyperreflective bands seen with High-Res OCT was almost identical (9.8 μm vs. 9.9 μm) to a separation between two mitochondria-rich sublayers. One was found at the outer edge of the inner nuclear layer (INL), in cells that were not determined, and the other at the level of the photoreceptor terminals. Further, mitochondria-rich and -poor fine sublayers formed by interneuron neurites did not correspond precisely to High-Res OCT bands. This suggests the presence of features possibly requiring higher axial resolution, optimized scan quality, and better focusing of optical plane (close to OPL). More specimens will be helpful in elucidating

Table 6. Comparison Between Retinal Band Visibility at 2 mm Nasal From the Fovea Between ART 9 and ART 100 Foveal Line Scans (n) in Healthy Young Adult Eyes (n = 11)

Retinal band	ART 9	ART 100	P
VRI	11	11	1.0
ILM	11	10	0.53
NFL	7	9	0.43
GCL	10	11	0.53
IPL-1	10	11	0.53
IPL-2	8	11	0.51
IPL-3	6	10	0.06
IPL-4	4	9	0.03
IPL-5	6	10	0.06
INL	10	11	0.53
OPL-1	7	8	0.65
OPL-2	5	11	0.02
HFL	7	11	0.13
ONL	11	11	1.00
ELM	11	11	1.00
MZ	11	11	1.00
EZ	11	11	1.00
OSIZ-1	10	11	0.53
OSIZ-2	11	11	1.00
RPE-1	11	10	0.53
RPE-2	10	9	0.53
RPE-3	9	9	1.00
RPE-4	9	11	0.51
RPE-5	9	10	0.53
BM	11	11	1.0
CC	11	11	1.0
CH	11	11	1.0

BM, Bruch membrane; CC, choriocapillaris; CH, choroid. GCL, ganglion-cell layer; HFL, Henle fiber layer; ILM, internal limiting membrane; MZ, myoid zone; NFL, nerve fiber layer; ONL, outer nuclear layer; VRI, vitreoretinal interface.

reflectivity OPL sources, including mitochondria and glial processes, of importance because OPL subsidence and hyperreflectivity are well documented in human disease.^{70,71} OPL ultrastructure for OCT validation has been reported for pig and mouse,^{72,73} two laboratory species that differ from humans in photoreceptor content and distribution.

Our nomenclature treats the EZ as a band with a thickness, and anterior and posterior boundaries, rather than a line. The EZ is considered an important biomarker in AMD trials, and mitochondria-targeting therapies are in development.^{74,75} Evidence for mitochondria as *in vivo* signal sources at the EZ is strong. Electron microscopy of human AMD retina

Table 7. Differences in Retinal Band Visibility Between Young (n = 10) and Aged (n = 22) Healthy Adults and Between Healthy Aged, eAMD (n = 17) and iAMD (n = 15) Eyes

Retinal band	Young vs. Aged p	Healthy Aged vs. eAMD vs. iAMD p
VRI	1.0	1.0
ILM	0.25	0.50
NFL	0.56	0.94
GCL	0.03	0.33
IPL-1	0.71	0.74
IPL-2	0.02	0.16
IPL-3	0.37	0.54
IPL-4	0.28	0.66
IPL-5	0.27	0.60
INL	0.21	0.12
OPL-1	0.61	0.28
OPL-2	0.06	0.50
HFL	0.13	0.65
ONL	1.00	1.00
ELM	1.00	0.27
MZ	1.00	0.27
EZ	0.51	0.34
OSIZ-1	0.18	0.02
OSIZ-2	0.01	<0.0001
RPE-1	0.01	<0.001
RPE-2	<0.0001	0.95
RPE-3	<0.0001	0.34
RPE-4	0.34	0.46
RPE-5	0.02	<0.001
BM	0.51	0.49
CC	1.00	0.31
CH	0.20	0.27

BM, Bruch membrane; CC, choriocapillaris; CH, choroid. GCL, ganglion-cell layer; HFL, Henle fiber layer; ILM, internal limiting membrane; MZ, myoid zone; NFL, nerve fiber layer; ONL, outer nuclear layer; VRI, vitreoretinal interface.

has shown that the normally long and thin ellipsoid mitochondria break up (fission) and translocate inwardly across the ELM as a group of small reflective organelles.^{5,13,76} Histological measures of IS lengths in normal retina align well with the tapered outer portion of the EZ.⁷⁷ In animal models, experiments using OCT as a readout have shown strain-specific diurnal differences in reflectivity⁴² and disrupted ellipsoid mitochondria with reduced reflectivity during hibernation.⁷⁸ It is important to note that EZ appearance is technology-dependent. Adaptive optics-assisted OCT reveals a thin reflective line, called the IS/OS junction, which is

attributed to a planar interface between the anatomical ellipsoid and OS.⁷⁹ It is possible that as resolution improved for SD-OCT, EZ thickness would converge on a single line. This convergence is not yet apparent with the device evaluated herein. We suggest that IS have complex optical properties including waveguiding, refraction, and reflection that may be differentially probed by various imaging technologies.^{1,80} This idea was demonstrated with multimodal imaging of outer retinal tubulation in advanced AMD.⁸¹ This scrolling of photoreceptors by Müller glia appeared hyperreflective on en face OCT and hyporeflective on adaptive optics scanning laser ophthalmoscopy.⁸¹

Outer Retina—Disambiguating the Third and Fourth Hyperreflective Bands

To handle the hyporeflective bared OS, we adopted the OSIZ terminology of Bloom and Singal (Fig. 8).²² We considered a combined OSIZ term appropriate because the OS and apical processes parallel each other in the axial dimension. Unlike these authors, we advance a bipartite rather than tripartite OSIZ. In our scheme, the inner OSIZ-1 is hyporeflective and the outer OSIZ-2 is hyperreflective and equivalent to the IZ of the IN-OCT consensus. The apical processes as fully realized by volume electron microscopy¹¹ resemble closely the IZ of SD-OCT (i.e., a feathery reflectivity emanating inwardly from the RPE-basal lamina-Bruch membrane band). This same ultrastructural study showed qualitatively that RPE apical processes paralleled most of the OS length but did not reach the ellipsoid. This research has also shown that ~2/3 of melanosomes in human RPE localize to the apical processes,^{11,48,82} as they do in other species. Melanosomes are experimentally proven reflectors⁸³ and may congregate near the base of the apical processes.

We do not use a third hyporeflective OSIZ outer band from the Bloom and Singal scheme. In their analysis of OCT volumes from patients with central serous retinopathy, this band either separated with detaching neurosensory retina or disappeared altogether.²² Rather, we believe that their OSIZ-3 is an apical portion of the RPE cell body, based on volume electron microscopy (Fig. 8) and emerging OCT technologies, as discussed below.⁸⁴ The two-part OSIZ terminology has two implications. First, it clearly demarcates the OS from the EZ anterior to it. Some grading schemes for OCT scans measure total EZ-RPE attenuation^{75,85} (i.e., the distance between segmented EZ and RPE bands), which necessarily includes the compositionally distinct OS. Second, the two-part OSIZ allows characteristic OS reflectivity signatures (e.g., curtain-like hyperreflectivity hanging from the EZ) to

be quantified and incorporated into pathophysiology models and outcome measures. To date these signatures are not well described or formalized^{86,87}; animal models may be helpful.⁸⁸ Repeating the Bloom and Singal paradigm with <3 μm OCT would be highly informative.

Our terminology embraces five alternating bands for the RPE cell body, based on volume electron microscopy (Fig. 8).¹¹ These reconstructions clarified in three dimensions what had been seen fragmentarily in two-dimensional images for years (i.e., a dense cushion of mitochondria at the basal RPE that diminished toward the apical aspect). Conversely, lipofuscin and melanolipofuscin of lysosomal origin and signal sources for fundus autofluorescence, were numerous in the apical cell body and absent from the basal one-fourth (Fig. 8). Thus two classes of membrane-bound organelles (lysosome-related and mitochondria) create two hyperreflective cushions in the RPE cell body (RPE-2 and RPE-4, respectively). We identified a narrow zone in the apical cell body with relatively few organelles as a candidate for a hyporeflective RPE-1, just external to the IZ of SD-OCT. A relative minimum in organelle packing at 7 μm external to the actin belt (Fig. 8) possibly corresponds to another hyporeflective band (RPE-3). Finally, our hyporeflective RPE-5 corresponds to the hyporeflective band vi recently identified using a 3 μm axial resolution prototype device and attributed to RPE basal infoldings in youth and BLamD in aging and AMD.^{23,37} Computational corrections for axial motion will allow a reappraisal of all bands in the RPE cell body.⁸⁴ Indeed initial images indicate that a band historically identified as rod OS tips or rod IZ (as opposed to cone OS tips or cone IZ) appears too close to the foveal center to represent rods, therefore possibly supporting our designation of a hyporeflective RPE-1.³⁷

Our nomenclature, supported by new comprehensive histology (Fig. 8), and taking into account known artifacts (Supplementary Table S1) does not support a nomenclature proposed by Cuenca et al.^{89,90} These authors provided exceptional immunofluorescence for organelle markers in neurosensory retina including ellipsoid mitochondria. For the four hyperreflective outer retinal bands, these authors proposed the ELM, EZ, RPE phagosome zone (a layer of ingested cone OS tips within the RPE cell bodies), and RPE mitochondria. We agree on the ELM and EZ as bands, and the basally located mitochondria as reflectivity sources within the RPE-BL-BrM band. We disagree with the “RPE phagosome zone,” due to several flaws in their study design and interpretation, and with the perspective of more recent data (Fig. 8). Cuenca et al relied exclusively on fluores-

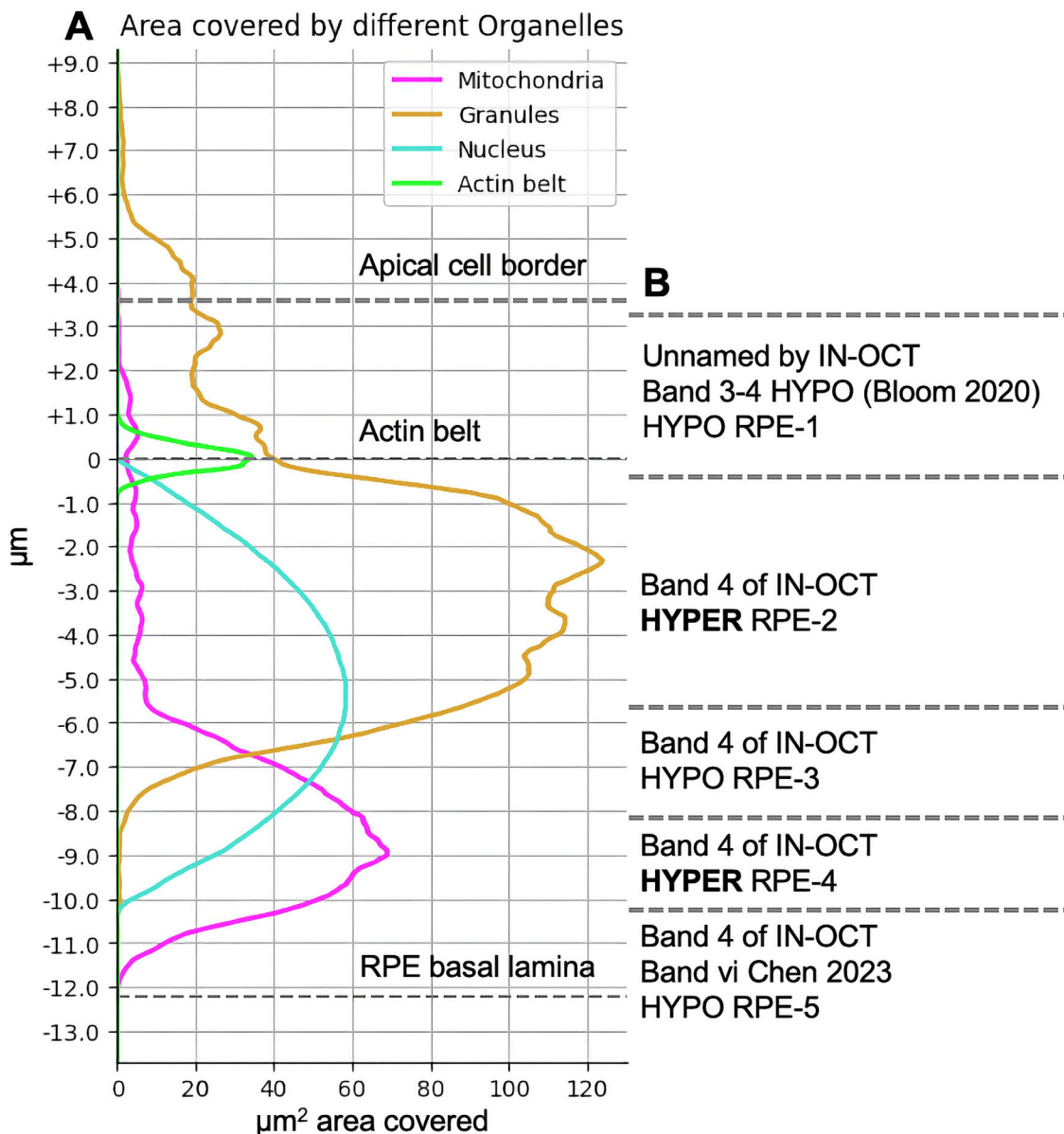


Figure 8. Harmonization of schemes for retinal pigment epithelium based on organelle distribution in volume electron microscopy. (A) Distribution of organelles in a single parafoveal RPE cell body of a 21-year-old male organ donor, as reconstructed by deep-learning assisted volume electron microscopy.¹¹ Apical processes are excluded. ED (electron-dense) organelles included lipofuscin, melanolipofuscin, and melanosomes. Y-axis shows depth along an apical-basal vertical axis, expressed as μm apical (+) or basal (−) to the actin cytoskeletal belt. Dashed lines indicate the approximate locations of apical border of the cell body, actin cytoskeletal belt, and basal lamina. X-axis shows average cross-section areas of organelles in μm^2 . Reproduced with slight modification from Lindell et al.¹¹ (B) Juxtaposed are corresponding band names in the presented nomenclature and the literature,^{20,22,23} as well as their reflectivity (HYPERreflective or HYPOreflective).

cent antibodies and laser confocal microscopy without correlative techniques for definitive localization of known RPE organelles. Further, no publications on RPE cell biology from the last 60 years that might have guided the explorations were cited. Thus, these authors misidentified the numerous ovoid lipofuscin/melanolipofuscin granules as melanosomes, a straightforward determination with fluorescence microscopy

or bright field microscopy of unstained tissue sections. Indeed, the summary schematic omitted altogether the RPE's characteristic spindle-shaped melanosomes that reside largely in the apical processes. Second, Cuenca et al.^{89,90} illustrated a solid mass on top of RPE cell bodies (their Figures 5 and 6) that they consider the cell body interior. In contrast, volume electron microscopy allows individual apical processes to be

followed through this mass, which we characterize as a “stepped-on lawn” due to compaction. Thus the “phagosome zone” does not represent cone OS tips inside the cell body, in our view, but rather OS tips outside the cell body, among the compacted apical processes.

We defined a structural foveal center as the point of the longest cone photoreceptors, signified by an inward rise of the ELM and EZ and reduced visibility of the EZ. In this sample, both bands were invisible in seven eyes (of 65 total), which also had mild AMD pathology. Others have reported that the ELM is present and unchanged in reflectivity until late in the course of AMD, supporting its use as an indicator of the foveal center.^{91,92} Our criteria identify a central bouquet, a region ~200 μ m in diameter,⁵⁴ comprised of the longest, thinnest cones interleaved with Müller glia. The ELM is an anatomic and physiologic boundary formed by junctional complexes between photoreceptors and Müller glia, which equal or exceed the number of central bouquet cones.^{55,93} The distinctive EZ appearance in the central bouquet (Fig. 1) may be attributable to an inward dispersion of mitochondria along the IS myoid that impacts refractive index gradients.^{5,94,95} Others⁹⁶ define the foveal center as the B-scan with maximum distance from EZ to IZ (which captures part of the OS) and minimum distance between the internal limiting membrane to RPE-BL-BrM complex, within the foveal pit. Whether OS length is a surrogate for peak cone density remains to be determined.^{58,97} In many eyes the rise of the ELM and EZ are vertically aligned with a fanning-out of cone nuclei in the outer nuclear layer (called a gateau),⁵⁴ seen well in histology⁹⁸ and adaptive optics assisted OCT.⁹⁹ As reviewed,⁴⁴ the spatial distributions of cones and rods, specified as a radially symmetric polar coordinate system secured at a precise foveal center, are decisive in mechanistic considerations of AMD’s earliest phases. OCT allows determination of a structural, cellular-level foveal center, in many eyes. This is a major reason for making OCT the anchor for all en face imaging modalities,³⁹ including adaptive optics assisted technologies.^{100–102}

Retinal Band Visibility

Using different ART modes for OCT acquisition impacts the inner retinal bands’ visibility, whereas the visibility of outer retinal bands appears unaffected. Reflectivity differences are small within in the IPL and OPL and large in the outer retina, as also seen in the LRP profile (Fig. 2). Visibility is improved

by the ART algorithm, which adds pixel-level data from every newly acquired B-scan to an existing stack of averaged B-scans (cumulative average). Increased resolution of the HR OCT device leads to the availability of more pixels (i.e. information) for the averaging process. Averaging multiple images can increase signal-to-noise ratio while reducing speckle, and brightness remains unaffected.¹⁰³ We hypothesize that the noise reduction entailed by higher ART values is responsible for the improved discernibility of the inner retinal layers. Further studies evaluating retinal band visibility in ART modes between 9 and 100 are warranted to determine the most practical ART setting.

Comparing retinal band visibility at ART9 among our diagnostic groups, we found better band visibility in young than in healthy aged adults. As mentioned above, the RPE’s organelles are organized in particular layers^{9–11} that generate hypo- and hyperreflective bands.⁵ With age or disease onset, this distinct organelle arrangement may become disorganized due to loss of polarity-maintenance mechanisms, consequently leading to changes on the OCT signal.^{104–106} These changes of OCT signal may hinder the identification of distinct bands. RPE-4 was generally discernable. RPE-2 and RPE-3 were more difficult. Simultaneous display of the LRP and B-scan allows inspection of the same band in adjacent locations, where it may be clearer. Thus, we assigned band visibility to grading locations with ambiguous reflectivity. We attribute the RPE-5 band to basal infoldings, a labyrinthine structure¹⁰⁷ in the basal RPE cell body, above the RPE basal lamina. This membrane specialization for uptake/transfer and fluid balance responsibilities of RPE recently became amenable to experimentation.¹⁰⁷

We identified differences in retinal band visibility between healthy aged, eAMD, and iAMD participants. Relative to healthy aged eyes, OSIZ-1-2 and RPE-1 were less visible and RPE-5 was more visible in eAMD and iAMD eyes. Visibility of the consensus IZ has been shown to deteriorate with age and to associate with delayed rod vision in healthy adults.⁶⁰ In addition to an age-dependent effect, AMD-related retinal structural alterations such as drusen and SDD may impact retinal band visibility mechanically.³ For example, the OCT light beam may strike OSIZ structures at different angles, degrading the generated reflectivity and making them less clearly separable from bands below and above.

Our proposed nomenclature posits five separate RPE bands (Fig. 8). RPE-5 is equivalent to the hyperreflective band “vi” previously attributed by Fujimoto and colleagues to the RPE’s basal infoldings.²³ Our analyses show that this band is less visible in healthy

aged compared to healthy young participants. This supports the previous findings²³ and fits with previous studies on mice showing that basal infoldings disappear with age as BLamD accumulates.^{108,109} In addition, we note greater RPE-5 visibility in iAMD eyes compared to eAMD eyes and healthy aged eyes. We suspect that this is due to the emergence of BLamD, which appears hyporeflective on OCT and is located posterior to the RPE.^{14,110}

Our methodology defines retinal bands as either visible or invisible. One needs to take into account that age- and disease-dependent structural alterations may lead to the approximation of two adjacent bands making it difficult or impossible to separate them.¹¹¹ For example, Emamverdi et al.¹¹¹ found that OS in the central area appeared thinner in eAMD compared to aged normal and iAMD eyes. The nonprogressive differences in thickness could represent an artifact of measurement technique, changes in OS themselves, or a complex relationship of OS with bands on either side of it, as discussed by these authors. For example, IZ disintegrity and shortening of IS that pulled up OS may have bared a greater length of OS (OSIZ-1 in the current scheme) captured in outer segment thickness measurements.¹¹¹

New Review Tools Leading to Improved Automatic Detection

How do we envision our review software being used, in the near term, while dissemination of $<3\text{ }\mu\text{m}$ OCT technology is in its early phases? Manual assessment of retinal band visibility using our nomenclature and review tool is designed for research purposes and is time-consuming. However, artificial intelligence and deep learning have gained in popularity and importance for image analysis in ophthalmology in recent years.^{112–114} Before employment in research and clinical care, algorithms need to be trained, tested, and validated.¹¹⁵ Is there a role for computer-assisted grading by expert readers in the training of automated algorithms?

Different approaches can be used to acquire images for algorithm training. First, large, unfiltered datasets like the UK Biobank, and the Age-Related Eye Disease Study offer a rich diversity of images, which is beneficial for training algorithms that adapt well to new, unseen data.^{32,116–118} The downside, however, is high variability in image quality and the spectrum of disease shown, which may eventually hinder algorithm training and performance.¹¹² These datasets are best used to train algorithms which are intended to assist in screening large samples for the presence of disease.

A second source for algorithm training data are clinical trial datasets.^{119,120} Advantages are that data are collected and curated with a specific research question in mind, and therefore image acquisition and processing follow standard operating procedures, including comprehensive metadata. This homogeneity facilitates learning and recognizing specific patterns. The generally smaller sample size warrants a risk for overfitting an algorithm, where the algorithm performs well in training, but struggles with new, unseen data.^{121–123} These data are most useful to train algorithms that recognize established imaging features from clinical trials in a real world setting.

The presented work on High-Res OCT and a custom review tool represents a third category of research that prioritizes high standards in patient selection, image acquisition, and postprocessing. Relying on skilled graders using a custom review tool designed for the specific purpose of creating detail-rich annotations, provides a strong foundation for machine learning models, enabling learn and generalize more effectively.^{124,125} One must recall that these data sets will be smaller than those described above, and possibly underpowered to detect some effects. These datasets are best used to establish and validate new imaging findings in health and disease.

Strengths, Weaknesses, Future Directions, and Conclusions

Several limitations need to be considered when evaluating this work. First, Heidelberg's High-Res OCT device is not yet commercially available and is deployed in research centers only. Once this and similar instruments are widely available, the proposed nomenclature can confirm its utility. Second, the dataset used to test and validate the nomenclature was limited to 11 healthy young eyes and 55 aged eyes in three diagnostic groups. Third, while processing High-Res OCT and conventional SD-OCT, the ImageJ review software currently works only with OCT format provided by Heidelberg Engineering devices. Fourth, although new histologic data has made it possible to reevaluate OCT nomenclature, extant volume electron microscopy studies involve small samples albeit yielding results consistent with prior literature. Fifth, we did not consider changes in retinal band visibility which may be attributable to differences in the posterior curvature. However, our review tool allows for the simultaneous comparison of retinal band visibility in different retinal loci. Posterior curvature-related changes in band visibility may be assessed by comparing band visibility of either side of the curvature. Sixth, we did not assess inter-reader reliability, which will be

included moving forward. In general, however, inter-reader reliability for band annotation has been shown to be superior in HR-OCT compared to conventional OCT devices.²⁵

Strengths of the study are the reliance on confirmed findings in histology, EM, and investigational OCT devices. Also, retinal bands with unclear subcellular correspondence were numbered to accommodate further adjustments when the anatomic structures are discovered. Future studies can focus on combining structural changes, as seen using this novel nomenclature, and visual function.

In conclusion, we offer a refinement of a 2014 consensus nomenclature for HR-OCT images, relying on discoveries in histology, electron microscopy, and investigational OCT devices, and validated with a novel review software. Further studies, investigating the relation between band visibility, thickness, integrity, and visual function may deepen our knowledge on how diseases develop and progress.

Acknowledgments

The authors thank Sophie Caujolle, PhD, Heidelberg Engineering, for assistance on the technical aspects of the High-Res OCT device.

Supported by NIH grants R01EY029595 (CO, CAC) and R01EY027948 (CAC); P30EY03039 (institutional); Dorsett Davis Discovery Fund (CO), and Alfreda J. Schueler Trust (CO); Deutsche Forschungsgemeinschaft (DFG) Grant GO 4009/1-1 (LG), Unrestricted funds to the Department of Ophthalmology and Visual Sciences (UAB) from Research to Prevent Blindness, Inc., and EyeSight Foundation of Alabama.

Disclosure: **L. Goerdt**, Novartis Pharma AG (R), Bayer Healthcare AG (R), BioEQ/Formycon (C); **T.A. Swain**, None; **D. Kar**, None; **G. McGwin**, None; **A. Berlin**, None; **M.E. Clark**, None; **C. Owsley**, Johnson & Johnson Vision (C); **K.R. Sloan**, None; **C.A. Curcio**, Heidelberg Engineering (R), Genentech/ Hoffman LaRoche (C), Apellis (C), Astellas (C), Boehringer Ingelheim (C), Character Biosciences (C), Osanni (C), Annexon (C), Mobius (C), and Ripple (C)

References

1. Miller DT, Kurokawa K. Cellular-scale imaging of transparent retinal structures and processes using adaptive optics optical coherence tomography. *Ann Rev Vis Sci*. 2020;6:115–148.
2. Spaide RF, Curcio CA. Anatomical correlates to the bands seen in the outer retina by optical coherence tomography: literature review and model. *Retina*. 2011;31:1609–1619.
3. Jacques SL. Optical properties of biological tissues: a review. *Phys Med Biol*. 2013;58:R37–R61.
4. Chýlek P, Zhan J. Absorption and scattering of light by small particles: the interference structure. *Appl Opt*. 1990;29:3984.
5. Litts KM, Zhang Y, Bailey Freund K, Curcio CA. Optical coherence tomography and histology of age-related macular degeneration support mitochondria as reflectivity sources. *Retina*. 2018;38:445–461.
6. Wilson JD, Bigelow CE, Calkins DJ, Foster TH. Light scattering from intact cells reports oxidative-stress-induced mitochondrial swelling. *Biophys J*. 2005;88:2929–2938.
7. Wilson JD, Cottrell WJ, Foster TH. Index-of-refraction-dependent subcellular light scattering observed with organelle-specific dyes. *J Biomed Opt*. 2007;12:014010.
8. Curcio CA, Messinger JD, Sloan KR, Mitra A, McGwin G, Spaide RF. Human Chorioretinal Layer Thicknesses Measured in Macula-wide, High-Resolution Histologic Sections. *Invest Ophthalmol Vis Sci*. 2011;52:3943.
9. Pollreisz A, Reiter GS, Bogunovic H, et al. Topographic distribution and progression of soft drusen volume in age-related macular degeneration implicate neurobiology of fovea. *Invest Ophthalmol Vis Sci*. 2021;62.
10. Bermond K, Wobbe C, Tarau IS, et al. Autofluorescent granules of the human retinal pigment epithelium: phenotypes, intracellular distribution, and age-related topography. *Investigative Ophthalmology and Visual Science*. 2020;61.
11. Lindell M, Kar D, Sedova A, et al. Volumetric Reconstruction of a Human Retinal Pigment Epithelial Cell Reveals Specialized Membranes and Polarized Distribution of Organelles. *Investigative Ophthalmology & Visual Science*. 2023;64:35.
12. Litts KM, Messinger JD, Dellatorre K, Yannuzzi LA, Freund KB, Curcio CA. Clinicopathological Correlation of Outer Retinal Tubulation in Age-Related Macular Degeneration. *JAMA Ophthalmology* 2015;133:609.
13. Schaal KB, Freund KB, Litts KM, Zhang Y, Messinger JD, Curcio CA. Outer retinal tubulation in advanced age-related macular degeneration. *Retina* 2015;35:1339–1350.

14. Sura AA, Chen L, Messinger JD, et al. Measuring the contributions of basal laminar deposit and bruch's membrane in age-related macular degeneration. *Investigative Ophthalmology and Visual Science* 2020;61(13):19.
15. Wang JJ, Rochtchina E, Lee AJ, et al. Ten-year incidence and progression of age-related maculopathy: the blue Mountains Eye Study. *Ophthalmology* 2007;114:92–98.
16. Joachim N, Mitchell P, Kifley A, Rochtchina E, Hong T, Wang JJ. Incidence and progression of geographic atrophy: observations from a population-based cohort. *Ophthalmology*. 2013;120:2042–2050.
17. Chen L, Messinger JD, Sloan KR, et al. Abundance and multimodal visibility of soft drusen in early age-related macular degeneration - a clinicopathologic correlation. *Retina*. 2020;1644–1648.
18. Chen L, Messinger JD, Kar D, Duncan JL, Curcio CA. Biometrics, impact, and significance of basal linear deposit and subretinal drusenoid deposit in age-related macular degeneration. *Investigative Ophthalmology and Visual Science*. 2021;62(1):33.
19. Chen L, Yang P, Curcio CA. Visualizing lipid behind the retina in aging and age-related macular degeneration, via indocyanine green angiography (ASHS-LIA). *Eye*. 2022;36:1735–1746.
20. Staurenghi G, Sadda S, Chakravarthy U, Spaide RF. Proposed lexicon for anatomic landmarks in normal posterior segment spectral-domain optical coherence tomography: the IN•OCT consensus. *Ophthalmology*. 2014;121:1572–1578.
21. Kar D, Kim YJ, Packer O, et al. Volume electron microscopy reveals human retinal mitochondria that align with reflective bands in optical coherence tomography [Invited]. *Biomed Opt Express*. 2023;14:5512–5527.
22. Bloom SM, Singal IP. Revised classification of the optical coherence tomography outer retinal bands based on central serous chorioretinopathy analysis. *Retina*. 2020;00:188.
23. Chen S, Abu-Qamar O, Kar D, et al. Ultrahigh Resolution OCT Markers of Normal Aging and Early Age-related Macular Degeneration. *Ophthalmology Science*. 2023;3.
24. Ghassabi Z, Kuranov RV, Schuman JS, et al. In Vivo Sublayer Analysis of Human Retinal Inner Plexiform Layer Obtained by Visible-Light Optical Coherence Tomography. *Investigative Ophthalmology & Visual Science*. 2022;63:18.
25. von der Emde L, Sassmannshausen M, Morelle O, et al. Reliability of retinal layer annotation with a novel, high-resolution optical coherence tomography device: a comparative study. *Bioengineering (Basel)*. 2023;10.
26. Frank S, Reiter GS, Leingang O, et al. Advances in photoreceptor and retinal pigment epithelium quantifications in intermediate AMD: high-res versus standard SPECTRALIS OCT. *Retina*. 2024.
27. Mahmoudi A, Corradetti G, Emamverdi M, et al. Atrophic Lesions Associated with Age-Related Macular Degeneration. *Ophthalmology Retina*. 2024;8:367–375.
28. Lad EM, Sleiman K, Banks DL, et al. Machine Learning OCT Predictors of Progression from Intermediate Age-Related Macular Degeneration to Geographic Atrophy and Vision Loss. *Ophthalmology Science*. 2022;2:100160.
29. Sleiman K, Veerappan M, Winter KP, et al. Optical Coherence Tomography Predictors of Risk for Progression to Non-Neovascular Atrophic Age-Related Macular Degeneration. *Ophthalmology*. 2017;124:1764–1777.
30. Bogunovic H, Montuoro A, Baratsits M, et al. Machine Learning of the Progression of Intermediate Age-Related Macular Degeneration Based on OCT Imaging. *Investigative Ophthalmology & Visual Science*. 2017;58:BIO141.
31. Dow ER, Jeong HK, Katz EA, et al. A Deep-Learning Algorithm to Predict Short-Term Progression to Geographic Atrophy on Spectral-Domain Optical Coherence Tomography. *JAMA Ophthalmology*. 2023;141:1052.
32. Bhuiyan A, Wong TY, Ting DSW, Govindaiah A, Souied EH, Smith RT. Artificial Intelligence to Stratify Severity of Age-Related Macular Degeneration (AMD) and Predict Risk of Progression to Late AMD. *Translational Vision Science & Technology*. 2020;9:25.
33. Schmidt-Erfurth U, Bogunovic H, Grechenig C, et al. Role of Deep Learning–Quantified Hyper-reflective Foci for the Prediction of Geographic Atrophy Progression. *American Journal of Ophthalmology*. 2020;216:257–270.
34. Kalra G, Cetin H, Whitney J, et al. Automated Identification and Segmentation of Ellipsoid Zone At-Risk Using Deep Learning on SD-OCT for Predicting Progression in Dry AMD. *Diagnostics*. 2023;13.
35. Abraham JR, Jaffe GJ, Kaiser PK, et al. Impact of Baseline Quantitative OCT Features on Response to Risuteganib for the Treatment of Dry Age-Related Macular Degeneration. *Ophthalmology Retina*. 2022;6:1019–1027.

36. Reche J, Stocker AB, Henchoz V, et al. High-Resolution Optical Coherence Tomography in Healthy Individuals Provides Resolution at the Cellular and Subcellular Levels. *Translational Vision Science and Technology*. 2023;12.
37. Won J, Takahashi H, Ploner SB, et al. Topographic Measurement of the Subretinal Pigment Epithelium Space in Normal Aging and Age-Related Macular Degeneration Using High-Resolution OCT. *Invest Ophthalmol Vis Sci*. 2024.
38. Sadda SR, Guymer R, Holz FG, et al. Consensus definition for atrophy associated with age-related macular degeneration on OCT: classification of atrophy report 3. *Ophthalmology*. 2018;125:537–548.
39. Holz FG, Sadda SR, Staurenghi G, et al. Imaging Protocols in Clinical Studies in Advanced Age-Related Macular Degeneration. *Ophthalmology*. 2017;124:464–478.
40. Guymer RH, Rosenfeld PJ, Curcio CA, et al. Incomplete retinal pigment epithelial and outer retinal atrophy in age-related macular degeneration: classification of atrophy meeting report 4. *Ophthalmology*. 2020;127:394–409.
41. Chen L, Messinger JD, Sloan KR, et al. Nonexudative Macular Neovascularization Supporting Outer Retina in Age-Related Macular Degeneration. *Ophthalmology*. 2020;127:931–947.
42. Berkowitz BA, Podolsky RH, Childers KL, et al. Functional changes within the rod inner segment ellipsoid in wildtype mice: an optical coherence tomography and electron microscopy study. *Investigative Ophthalmology & Visual Science*. 2022;63:8.
43. Berkowitz BA, Podolsky RH, Qian H, et al. Mitochondrial Respiration in Outer Retina Contributes to Light-Evoked Increase in Hydration In Vivo. *Investigative Ophthalmology & Visual Science*. 2018;59:5957.
44. Curcio CA, Kar D, Owsley C, Sloan KR, Ach T. Age-Related Macular Degeneration, a Mathematically Tractable Disease. *Investigative Ophthalmology & Visual Science*. 2024;65:4.
45. Haverkamp S, Haeseler F, Hendrickson A. A comparison of immunocytochemical markers to identify bipolar cell types in human and monkey retina. *Visual Neuroscience*. 2003;20:589–600.
46. Wässle H. Parallel processing in the mammalian retina. *Nat Rev Neurosci*. 2004;5:747–757.
47. Tanna H, Dubis AM, Ayub N, et al. Retinal imaging using commercial broadband optical coherence tomography. *British Journal of Ophthalmology*. 2010;94:372–376.
48. Pollreisz A, Neschi M, Sloan KR, et al. Atlas of Human Retinal Pigment Epithelium Organelles Significant for Clinical Imaging. *Investigative Ophthalmology & Visual Science*. 2020;61:13.
49. Zhang T, Kho AM, Srinivasan VJ. Improving visible light OCT of the human retina with rapid spectral shaping and axial tracking. *Biomed Opt Express*. 2019;10:2918–2931.
50. Berlin A, Cabral D, Chen L, et al. Histology of Type 3 Macular Neovascularization and Microvascular Anomalies in Treated Age-Related Macular Degeneration. *Ophthalmology Science*. 2023;3:100280.
51. Zanzottera EC, Messinger JD, Ach T, Smith RT, Freund KB, Curcio CA. The Project MACULA Retinal Pigment Epithelium Grading System for Histology and Optical Coherence Tomography in Age-Related Macular Degeneration. *Investigative Ophthalmology & Visual Science*. 2015;56:3253.
52. Li M, Dolz-Marco R, Huisings CE, et al. Clinicopathologic correlation of geographic atrophy secondary to age-related macular degeneration. *Retina*. 2019;39:802–816.
53. Chen L, Messinger JD, Zhang Y, Spaide RF, Freund KB, Curcio CA. Subretinal drusenoid deposit in age-related macular degeneration: histologic insights into initiation, progression to atrophy, and imaging. *RETINA*. 2020;40.
54. Rochon-Duvigneaud A. Les yeux et la vision des vertébrés. 1943.
55. Kar D, Singireddy R, Kim YJ, et al. Unusual morphology of foveal Müller glia in an adult human born pre-term. *Frontiers in Cellular Neuroscience*. 2024;18.
56. Huang Y, Cideciyan AV, Alemán TS, et al. Optical coherence tomography (OCT) abnormalities in rhodopsin mutant transgenic swine with retinal degeneration. *Exp Eye Res*. 2000;70:247–251.
57. Huang Y, Cideciyan AV, Papastergiou GI, et al. Relation of optical coherence tomography to microanatomy in normal and rd chickens. *Invest Ophthalmol Vis Sci*. 1998;39:2405–2416.
58. Wilk MA, McAllister JT, Cooper RF, et al. Relationship Between Foveal Cone Specialization and Pit Morphology in Albinism. *Investigative Ophthalmology & Visual Science*. 2014;55:4186.
59. Schindelin J, Arganda-Carreras I, Frise E, et al. Fiji: an open-source platform for biological-image analysis. *Nature Methods*. 2012;9:676–682.
60. Berlin A, Matney E, Jones SG, et al. Discernibility of the Interdigitation Zone (IZ), a Potential Optical Coherence Tomography (OCT) Biomarker

- for Visual Dysfunction in Aging. *Curr Eye Res.* 2023;48:1050–1056.
61. Curcio CA, Sloan KR, Kalina RE, Hendrickson AE. Human Photoreceptor Topography. *The Journal of comparative Neurology*. 1990;292:497–523.
62. Owsley C, McGwin G, Jr, Swain TA, et al. Outer Retinal Thickness Is Associated With Cognitive Function in Normal Aging to Intermediate Age-Related Macular Degeneration. *Invest Ophthalmol Vis Sci*. 2024;65.
63. Age related Eye Disease Study Research Group. A simplified severity scale for age-related macular degeneration: ards report no. 18. *Arch Ophthalmol*. 2005;123:1570–1574.
64. Echols BS, Clark ME, Swain TA, et al. Hyperreflective Foci and Specks Are Associated with Delayed Rod-Mediated Dark Adaptation in Non-neovascular Age-Related Macular Degeneration. *Ophthalmology Retina*. 2020;4:1059–1068.
65. Kho A, Srinivasan VJ. Compensating spatially dependent dispersion in visible light OCT. *Optics Letters*. 2019;44.
66. Szkulmowski M, Gorczynska I, Szlag D, Sylwestrzak M, Kowalczyk A, Wojtkowski M. Efficient reduction of speckle noise in Optical Coherence Tomography. *Opt Express*. 2012;20:1337–1359.
67. Sanes JR, Masland RH. The Types of Retinal Ganglion Cells: Current Status and Implications for Neuronal Classification. *Annual Review of Neuroscience*. 2015;38:221–246.
68. Sernagor E, Eglen SJ, Wong ROL. Development of Retinal Ganglion Cell Structure and Function. *Prog Retin Eye Res*. 2001;20:139–174.
69. Wagner SK, Fu DJ, Faes L, et al. Insights into Systemic Disease through Retinal Imaging-Based Oculomics. *Translational Vision Science & Technology*. 2020;9:6.
70. Chu YK, Hong YT, Byeon SH, Kwon OW. In vivo detection of acute ischemic damages in retinal arterial occlusion with optical coherence tomography: a “prominent middle limiting membrane sign”. *Retina*. 2013;33:2110–2117.
71. Wu Z, Goh KL, Hodgson LAB, Guymer RH. Incomplete Retinal Pigment Epithelial and Outer Retinal Atrophy: Longitudinal Evaluation in Age-Related Macular Degeneration. *Ophthalmology*. 2023;130:205–212.
72. Xie W, Zhao M, Tsai S-H, et al. Correlation of spectral domain optical coherence tomography with histology and electron microscopy in the porcine retina. *Experimental Eye Research*. 2018;177:181–190.
73. Chauhan P, Kho AM, Srinivasan VJ. From Soma to Synapse: Imaging Age-Related Rod Photoreceptor Changes in the Mouse with Visible Light OCT. *Ophthalmology Science*. 2023;3:100321.
74. Ehlers JP, Zahid R, Kaiser PK, et al. Longitudinal Assessment of Ellipsoid Zone Integrity, Subretinal Hyperreflective Material, and Subretinal Pigment Epithelium Disease in Neovascular Age-Related Macular Degeneration. *Ophthalmol Retina*. 2021;5:1204–1213.
75. Yordi S, Cakir Y, Kalra G, et al. Ellipsoid Zone Integrity and Visual Function in Dry Age-Related Macular Degeneration. *J Pers Med*. 2024;14.
76. Dolz-Marcos R, Litts KM, Tan ACS, Freund KB, Curcio CA. The Evolution of Outer Retinal Tubulation, a Neurodegeneration and Gliosis Prominent in Macular Diseases. *Ophthalmology*. 2017;124:1353–1367.
77. Ross DH, Clark ME, Godara P, et al. RefMoB, a reflectivity feature model-based automated method for measuring four outer retinal hyperreflective bands in optical coherence tomography. *Investigative Ophthalmology and Visual Science*. 2015;56:4166–4176.
78. Sajdak BS, Bell BA, Lewis TR, et al. Assessment of Outer Retinal Remodeling in the Hibernating 13-Lined Ground Squirrel. *Investigative Ophthalmology & Visual Science*. 2018;59:2538.
79. Jonnal RS, Kocaoglu OP, Zawadzki RJ, Lee SH, Werner JS, Miller DT. The cellular origins of the outer retinal bands in optical coherence tomography images. *Investigative Ophthalmology and Visual Science*. 2014;55:7904–7918.
80. Ball JM, Chen S, Li W. Mitochondria in cone photoreceptors act as microlenses to enhance photon delivery and confer directional sensitivity to light. *Science Advances*. 2022;8.
81. Litts KM, Wang X, Clark ME, et al. Exploring photoreceptor reflectivity through multimodal imaging of outer retinal tubulation in advanced age-related macular degeneration. *Retina*. 2017;37:978–988.
82. Pollreisz A, Messinger JD, Sloan KR, et al. Visualizing melanosomes, lipofuscin, and melanolipofuscin in human retinal pigment epithelium using serial block face scanning electron microscopy. *Experimental Eye Research*. 2018;166:131–139.
83. Zhang Q-X, Lu R-W, Messinger JD, Curcio CA, Guarcello V, Yao X-C. In vivo Optical Coherence Tomography of Light-Driven Melanosome Translocation in Retinal Pigment Epithelium. *Scientific Reports*. 2013;3.
84. Won J, Takahashi H, Ploner SB, et al. Topographic measurement of the sub-retinal pig-

- ment epithelium space in normal aging and age-related macular degeneration using high-resolution OCT. *Invest Ophthalmol Vis Sci*. 2024.
85. Ehlers JP, Lunasco LM, Yordi S, et al. Compartmental Exudative Dynamics in Neovascular Age-Related Macular Degeneration: Volumetric Outcomes and Impact of Volatility in a Phase III Clinical Trial. *Ophthalmol Retina*. 2024.
 86. Heath Jeffery RC, Lo J, Thompson JA, et al. Analysis of the Outer Retinal Bands in ABCA4 and PRPH2-Associated Retinopathy using OCT. *Ophthalmol Retina*. 2024;8:174–183.
 87. Shields CL, Kaliki S, Rojanaporn D, Ferenczy SR, Shields JA. Enhanced Depth Imaging Optical Coherence Tomography of Small Choroidal Melanoma. *Archives of Ophthalmology*. 2012;130:850.
 88. Bonilha VL, Bell BA, Rayborn ME, et al. Loss of DJ-1 elicits retinal abnormalities, visual dysfunction, and increased oxidative stress in mice. *Exp Eye Res*. 2015;139:22–36.
 89. Cuenca N, Ortúñoz-Lizarán I, Pinilla I. Cellular Characterization of OCT and Outer Retinal Bands Using Specific Immunohistochemistry Markers and Clinical Implications. *Ophthalmology*. 2018;125:407–422.
 90. Cuenca N, Ortúñoz-Lizarán I, Sánchez-Sáez X, et al. Interpretation of OCT and OCTA images from a histological approach: Clinical and experimental implications. *Prog Retin Eye Res*. 2020;77:100828.
 91. Gin TJ, Wu Z, Chew SKH, Guymer RH, Luu CD. Quantitative analysis of the ellipsoid zone intensity in phenotypic variations of intermediate age-related macular degeneration. *Investigative Ophthalmology and Visual Science*. 2017;58:2079–2086.
 92. Wu Z, Ayton LN, Guymer RH, Luu CD. Relationship between the second reflective band on optical coherence tomography and multifocal electroretinography in age-related macular degeneration. *Investigative Ophthalmology and Visual Science*. 2013;54:2800–2806.
 93. Ahmad KM, Klug K, Herr S, Sterling P, Schein S. Cell density ratios in a foveal patch in macaque retina. *Visual Neuroscience*. 2003;20:189–209.
 94. Yamada E. Some structural features of the fovea centralis in the human retina. *Arch Ophthalmol*. 1969;82:151–159.
 95. Hoang QV, Linsenmeier RA, Chung CK, Curcio CA. Photoreceptor inner segments in monkey and human retina: mitochondrial density, optics, and regional variation. *Vis Neurosci*. 2002;19:395–407.
 96. Pedersen HR, Neitz M, Gilson SJ, et al. The Cone Photoreceptor Mosaic in Aniridia. *Ophthalmology Retina*. 2019;3:523–534.
 97. Domdei N, Ameln J, Gutnikov A, et al. Cone Density Is Correlated to Outer Segment Length and Retinal Thickness in the Human Foveola. *Investigative Ophthalmology & Visual Science*. 2023;64:11.
 98. Govetto A, Bhavsar KV, Virgili G, et al. Tractonal Abnormalities of the Central Foveal Bouquet in Epiretinal Membranes: Clinical Spectrum and Pathophysiological Perspectives. *Am J Ophthalmol*. 2017;184:167–180.
 99. Kadomoto S, Muraoka Y, Uji A, et al. Human Foveal Cone and Müller Cells Examined by Adaptive Optics Optical Coherence Tomography. *Translational Vision Science & Technology*. 2021;10:17.
 100. Liu Z, Aghayee S, Soltanian-Zadeh S, et al. Quantification of Human Photoreceptor—Retinal Pigment Epithelium Macular Topography with Adaptive Optics—Optical Coherence Tomography. *Diagnostics*. 2024;14.
 101. Zhang T, Godara P, Blanco ER, et al. Variability in Human Cone Topography Assessed by Adaptive Optics Scanning Laser Ophthalmoscopy. *American Journal of Ophthalmology*. 2015;160:290–300.e291.
 102. Baraas RC, Pedersen HR, Knoblauch K, Gilson SJ. Human Foveal Cone and RPE Cell Topographies and Their Correspondence With Foveal Shape. *Investigative Ophthalmology & Visual Science*. 2022;63:8.
 103. Podkowinski D, Sharian Varnousfaderani E, Simader C, et al. Impact of B-Scan Averaging on Spectralis Optical Coherence Tomography Image Quality before and after Cataract Surgery. *Journal of Ophthalmology*. 2017;2017:1–8.
 104. Gambril JA, Sloan KR, Swain TA, et al. Quantifying Retinal Pigment Epithelium Dysmorphia and Loss of Histologic Autofluorescence in Age-Related Macular Degeneration. *Investigative Ophthalmology & Visual Science*. 2019;60:2481.
 105. Feeney-Burns L, Hilderbrand ES, Eldridge S. Aging human RPE: Morphometric analysis of macular, equatorial, and peripheral cells. *Investigative Ophthalmology and Visual Science*. 1984;25:195–200.
 106. Tarau I-S, Berlin A, Curcio CA, Ach T. The Cytoskeleton of the Retinal Pigment Epithelium: from Normal Aging to Age-Related Macular

- Degeneration. *International Journal of Molecular Sciences*. 2019;20:3578.
107. Hayes MJ, Burgoine T, Wavre-Shapton ST, Tolmachova T, Seabra MC, Futter CE. Remodeling of the Basal Labyrinth of Retinal Pigment Epithelial Cells With Osmotic Challenge, Age, and Disease. *Investigative Ophthalmology & Visual Science*. 2019;60:2515.
108. Mishima H, Kondo K. Ultrastructure of age changes in the basal infoldings of aged mouse retinal pigment epithelium. *Exp Eye Res*. 1981;33:75–84.
109. Katz ML, Robison WG, Jr. Senescence and the retinal pigment epithelium: alterations in basal plasma membrane morphology. *Mech Ageing Dev*. 1985;30:99–105.
110. Curcio CA, Millican CL. Basal linear deposit and large drusen are specific for early age-related maculopathy. *Archives of ophthalmology*. 1999;117:329–339.
111. Emamverdi M, Vatanatham C, Fasih-Ahmad S, et al. Probing Deposit-Driven Age-Related Macular Degeneration Via Thicknesses of Outer Retinal Bands and Choroid: ALSTAR2 Baseline. *Investigative Ophthalmology & Visual Science*. 2024;65:17.
112. De Fauw J, Ledsam JR, Romera-Paredes B, et al. Clinically applicable deep learning for diagnosis and referral in retinal disease. *Nature Medicine*. 2018;24:1342–1350.
113. Burlina PM, Joshi N, Pekala M, Pacheco KD, Freund DE, Bressler NM. Automated Grading of Age-Related Macular Degeneration From Color Fundus Images Using Deep Convolutional Neural Networks. *JAMA Ophthalmol*. 2017;135:1170–1176.
114. Faes L, Liu X, Wagner SK, et al. A Clinician's Guide to Artificial Intelligence: How to Critically Appraise Machine Learning Studies. *Translational Vision Science & Technology*. 2020;9.
115. Liu X, Faes L, Kale AU, et al. A comparison of deep learning performance against health-care professionals in detecting diseases from medical imaging: a systematic review and meta-analysis. *The Lancet Digital Health*. 2019;1:e271–e297.
116. Sudlow C, Gallacher J, Allen N, et al. UK Biobank: An Open Access Resource for Identifying the Causes of a Wide Range of Complex Diseases of Middle and Old Age. *PLOS Medicine*. 2015;12:e1001779.
117. Ting DSW, Pasquale LR, Peng L, et al. Artificial intelligence and deep learning in ophthalmology. *British Journal of Ophthalmology*. 2019;103:167–175.
118. Lavigne M, Mussa F, Creatore MI, Hoffman SJ, Buckeridge DL. A population health perspective on artificial intelligence. *Healthcare Management Forum*. 2019;32:173–177.
119. Schmidt-Erfurth U, Waldstein SM. A paradigm shift in imaging biomarkers in neovascular age-related macular degeneration. *Progress in Retinal and Eye Research*. 2016;50:1–24.
120. Schmidt-Erfurth U, Waldstein SM, Klimscha S, et al. Prediction of Individual Disease Conversion in Early AMD Using Artificial Intelligence. *Investigative Ophthalmology & Visual Science*. 2018;59:3199–3208.
121. Mutasa S, Sun S, Ha R. Understanding artificial intelligence based radiology studies: What is overfitting? *Clin Imaging*. 2020;65:96–99.
122. Handelman GS, Kok HK, Chandra RV, et al. Peering Into the Black Box of Artificial Intelligence: Evaluation Metrics of Machine Learning Methods. *AJR Am J Roentgenol*. 2019;212:38–43.
123. Rajkomar A, Oren E, Chen K, et al. Scalable and accurate deep learning with electronic health records. *npj Digital Medicine*. 2018;1.
124. Maloca PM, Lee AY, De Carvalho ER, et al. Validation of automated artificial intelligence segmentation of optical coherence tomography images. *PLOS ONE*. 2019;14:e0220063.
125. Maloca PM, Pfau M, Janeschitz-Kriegl L, et al. Human selection bias drives the linear nature of the more ground truth effect in explainable deep learning optical coherence tomography image segmentation. *Journal of Biophotonics*. 2023.
126. Torczynski E, Tso MO. The architecture of the choriocapillaris at the posterior pole. *Am J Ophthalmol*. 1976;81:428–440.